Reconnection Inside a Dipolarization Front of a Diverging Earthward Fast Flow

M. Hosner, R. Nakamura, D. Schmid, T. Nakamura, E. Panov, M. Volwerk, Z. Vörös, O. Roberts, K. Blasl, A. Settino, et al.

JGR Space Physics

RESEARCH ARTICLE
10.1029/2023JA031976

Key Points:

- A thin current sheet inside a dipolarization front, embedded in a diverging flow is analyzed using a polynomial reconstruction technique
- Transient reconnection event is detected in a high magnetic shear region, where the magnetic field is deflected due to duskward fast plasma flow
- The reconstructed current sheet has a guide field of ∼1.8 the reconnecting component with normalized reconnection rate between 0.16 and 0.18

Supporting Information:

Supporting Information may be found in the online version of this article.

Correspondence to:

M. Hosner,
martin.hosner@oeaw.ac.at

Citation:

Hosner, M., Nakamura, R., Schmid, D., Nakamura, T. K. M., Panov, E. V., Volwerk, M., et al. (2024). Reconnection inside a dipolarization front of a diverging Earthward fast flow. *Journal of Geophysical Research: Space Physics*, *129*, e2023JA031976. https://doi.org/10.1029/2023JA031976

Received 6 AUG 2023
Accepted 5 DEC 2023

Reconnection Inside a Dipolarization Front of a Diverging Earthward Fast Flow

M. Hosner[1,2], R. Nakamura[1], D. Schmid[1], T. K. M. Nakamura[1,3], E. V. Panov[1], M. Volwerk[1], Z. Vörös[1,4], O. W. Roberts[1], K. A. Blasl[1,2], A. Settino[1], D. Korovinskiy[1], A. T. Marshall[5], R. E. Denton[6], J. L. Burch[7], B. L. Giles[8], R. B. Torbert[7,9], O. Le Contel[10], C. P. Escoubet[11], I. S. Dandouras[12], C. Carr[13], and A. N. Fazakerley[14]

[1]Space Research Institute, Austrian Academy of Sciences, Graz, Austria, [2]Institute of Physics, University of Graz, Graz, Austria, [3]Krimgen LLC, Hiroshima, Japan, [4]Institute of Earth Physics and Space Science, Sopron, Hungary, [5]Department of Physics and Astronomy, Rice University, Houston, TX, USA, [6]Department of Physics and Astronomy, Dartmouth College, Hanover, NH, USA, [7]Southwest Research Institute, San Antonio, TX, USA, [8]Goddard Space Flight Center, NASA, Greenbelt, MD, USA, [9]Space Science Center, University New Hampshire, Durham, NH, USA, [10]LPP, CNRS, Sorbonne Université, Université Paris-Saclay, Observatoire de Paris, Ecole Polytechnique, Institut Polytechnique de Paris, Paris, France, [11]ESTEC/ESA, Noordwijk, The Netherlands, [12]IRAP, Université de Toulouse/CNRS/UPS/CNES, Toulouse, France, [13]Imperial College London, London, UK, [14]Mullard Space Science Lab, Dorking, UK

Abstract We examine a Dipolarization Front (DF) event with an embedded electron diffusion region (EDR), observed by the Magnetospheric Multiscale (MMS) spacecraft on 08 September 2018 at 14:51:30 UT in the Earth's magnetotail by applying multi-scale multipoint analysis methods. In order to study the large-scale context of this DF, we use conjunction observations of the Cluster spacecraft together with MMS. A polynomial magnetic field reconstruction technique is applied to MMS data to characterize the embedded electron current sheet including its velocity and the X-line exhaust opening angle. Our results show that the MMS and Cluster spacecraft were located in two counter-rotating vortex flows, and such flows may distort a flux tube in a way that the local magnetic shear angle is increased and localized magnetic reconnection may be triggered. Using multi-point data from MMS we further show that the local normalized reconnection rate is in the range of $R \sim 0.16$ to 0.18. We find a highly asymmetric electron in- and outflow structure, consistent with previous simulations on strong guide-field reconnection events. This study shows that magnetic reconnection may not only take place at large-scale stable magnetopause or magnetotail current sheets but also in transient localized current sheets, produced as a consequence of the interaction between the fast Earthward flows and the Earth's dipole field.

Plain Language Summary Magnetic Reconnection is a key energy conversion process, where magnetic energy is converted into kinetic energy of plasma particles. During this process the magnetic field topology changes and the plasma particles decouple from the magnetic field in the so-called diffusion region and get accelerated, forming a fast outflow jet. Over the last decades, hints arise that reconnection can take place at many different places in the magnetosphere and also very locally and intermittently. Fast plasma flows in the Magnetotail, moving toward the Earth, are assumed to be a consequence of magnetic reconnection, and are often accompanied by dipolar-shaped magnetic flux bundles, embedded into them. The leading edges of such flux bundles are called dipolarization fronts (DF). In this work, we investigate a DF event, which hosts a diffusion region. First, we study the large-scale characteristics of the DF, by utilizing data from both the Magnetospheric Multiscale (MMS) and the Cluster mission, that observe different regions of the event almost simultaneously. Second, we performed a 3D magnetic field reconstruction technique and compared the results to MMS data, to investigate the event on small scales.

1. Introduction

In the near Earth magnetotail fast earthward-moving plasma flows are frequently observed, with velocities over 400 km/s and a duration of a few seconds (Baumjohann et al., 1990). These short-duration flows can be grouped together into ∼10 min lasting flow intervals, termed Bursty Bulk Flows (BBFs) (Angelopoulos et al., 1992), which are responsible for a major part of particle and plasma transport in the magnetotail toward the Earth (Angelopoulos et al., 1994). Sergeev et al. (1996) observed flux tubes with increased northward magnetic field

and decreased plasma density and pressure, which are embedded into such BBFs, and therefore are co-moving earthwards. The leading edge of such flux tubes is called a dipolarization front (DF) (Nakamura et al., 2002), which acts as the boundary between the hot but depleted plasma region within the dipolarizing flux bundle (Liu et al., 2013) and the cold but dense plasma region ahead. Therefore, in in situ measurements, they are identified by sharp northward magnetic field enhancements (positive B_Z in the Geocentric Solar Magnetic (GSM) component) and a strong density gradient. They exhibit a width of 2–3 R_E in dawn-dusk direction and 1.5–2 R_E in north-south direction (Nakamura, R. et al., 2004) (with R_E = 6,371 km being the Earth's Radius), have a typical thickness on the order of the ion inertial length and can traverse through the magnetotail over distances of more than 10 R_E (Runov et al., 2009).

With the use of the unprecedented high resolution plasma and field data of NASA's Magnetospheric Multiscale (MMS) mission (Burch et al., 2016), DFs were recently studied on scales smaller than ion scale (e.g., Liu, Fu, Viavads, et al., 2018; Liu, Fu, Xu, et al., 2018, Pan et al., 2018). While the front itself is an ion-scale structure, they can exhibit features on sub-ion scales such as electron-scale currents with both positive and negative $\mathbf{j}\cdot\mathbf{E}$ (Alqeeq et al., 2022) (with $\mathbf{j}$ being the current density and $\mathbf{E}$ the electric field), and lower hybrid drift instability-associated lower hybrid waves, which were observed in in situ measurements (Hosner et al., 2022; Le Contel et al., 2017; Pan et al., 2018) and simulations (e.g., Divin et al., 2015; Nakamura et al., 2019).

Marshall et al. (2020) have reported a dipolarization front event in the magnetotail, which shows several electron-scale features in combination. They observed a strong electron-carried current in a very thin and localized electron-scale current sheet. The electrons' bulk velocity reaches up to 5,000 km/s and they are violating ideal magnetohydrodynamics. The electron velocity distribution function within the current sheet has a distinct crescent shape, they observed highly agyrotropic electrons and high $\mathbf{j}\cdot\mathbf{E}'$ values (with $\mathbf{E}' = \mathbf{E} + (\mathbf{v}_e \times \mathbf{B})$ being the electric field in the electron frame). These signatures are typically interpreted as signs of an electron diffusion region (EDR). In their LMN coordinate system, they observed a switching of sign in the B_L component and a very small, yet finite B_N (where B_L is the reconnecting magnetic field component and B_N is the current sheet normal component). Therefore, they have not directly observed an X-line, however, they have concluded that magnetic reconnection is taking place within the DF due to the aforementioned features and MMS1 and MMS2 are very likely crossing close to or within the EDR, where electrons decouple from the surrounding magnetic field and are demagnetized. Another aspect that makes this event interesting, in particular when considering reconnection, is its proximity to Earth as it was observed at about −12 R_E tailwards. Also, this event was used as a benchmark for the single-spacecraft magnetic field reconstruction technique, which is based on solving the Grad-Shafranov equation, by Korovinskiy et al. (2023), who have also reported an X-line topology. Furthermore, this event was studied by Liu et al. (2022) using MMS data. They have confirmed the small-scale electron-carried current but have not considered magnetic reconnection as the source of acceleration, but local electrostatic potentials and associated electric fields. Based on the magnetic field data they have concluded that the plasma flow, into which this DF is embedded, is diverted due to plasma jet braking and thus distorts the earthward moving flux tube.

In the present work we revisit this unique event under the new light based on multi-point analysis at different scales. In terms of the MHD scale we compare and contrast DF and BBF observations between MMS and the Cluster 4 spacecraft (Escoubet et al., 2001) that were separated by only 2.6 R_E and likely observed the same DF event almost simultaneously. Another conjugate Cluster and MMS observation of the same BBF and DF (confirmed from the energetic electron observations but had no signatures of EDR) were studied by Nakamura et al. (2021), that took place about 30 min before the event, discussed in this paper, indicating that both spacecraft were located in a favorable constellation for the mesoscale comparisons of BBFs during this period. Comparing two missions' data allows us to gain information about the event at two different locations under slightly different circumstances to make statements about why magnetic reconnection takes place at MMS's location but not at Cluster's location. Furthermore, by applying the polynomial magnetic field reconstruction technique by Denton et al. (2020) to MMS data, we obtain information about the 3D magnetic field topology and its evolution in the vicinity of the MMS spacecraft during the DF (thin current sheet) crossing in order to examine the consistency of the event to be interpreted as magnetic reconnection.

2. Observation

On 08 September 2018 at 14:51 UT both the MMS and Cluster spacecraft (in the following we use “S/C” and “spacecraft” synonymously) were in the pre-midnight magnetotail at (−13.2, 5.5, 0.8) R_E and at (−14.7, 4.0,

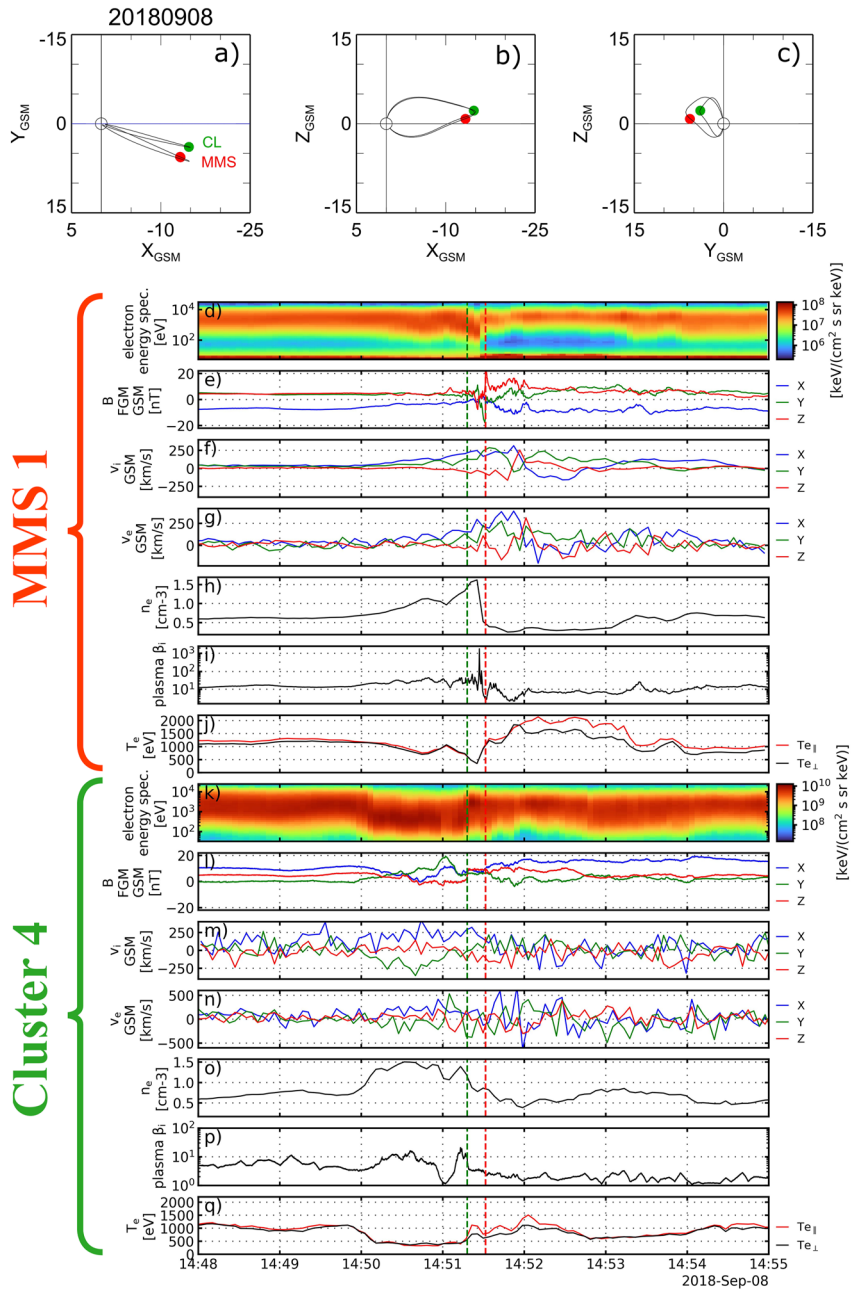

Figure 1. A seven-minute overview of MMS and Cluster 4 measurements around the dipolarization front. (a–c) MMS (red) and Cluster 4 (green) position with magnetic field lines from the TA15 model, (d–j) MMS (fast) survey mode data, (k–q) Cluster 4 data, (d) FPI electron omnidirectional energy spectrum, (e) FGM magnetic field, (f) FPI ion bulk velocity, (g) FPI electron bulk velocity, (h) FPI electron density, (i) ion plasma beta, (j) FPI perpendicular (black) and parallel (red) electron temperature, (k) PEACE electron omnidirectional energy spectrum, (l) FGM magnetic field, (m) CODIF ion bulk velocity, (n) PEACE electron bulk velocity, (o) PEACE electron density, (p) ion plasma beta, (q) PEACE perpendicular (black) and parallel (red) electron temperature.

2.3) R_E, respectively in the GSM coordinate system as shown in Figures 1a–1c. The red dot represents the MMS spacecraft and the green dot represents the Cluster 4 spacecraft. Also, based on the model of Tsyganenko and Andreeva (2015), in the following abbreviated as TA15, magnetic field lines are displayed as black curves.

In Figures 1d–1q the plasma and magnetic field observations between 14:48 and 14:54 UT, observed by MMS1 and Cluster 4 are shown. Figure 1e shows the 0.0625s (16 Hz) averaged MMS magnetic field data from the Flux

Gate Magnetometer (FGM) (Russell et al., 2016). The particle data in Figures 1d, 1f–1j are from the Fast Plasma Investigation (FPI) (Pollock et al., 2016), shown as 4.5s (0.22 Hz) averaged data. The Cluster magnetic field data, shown in Figure 1l, is obtained by the Flux Gate Magnetometer (FGM) (Balogh et al., 2001) with a time resolution of 0.015s (66.7 Hz). The ion velocity (Figure 1m) and pressure, used for the plasma beta (Figure 1p), are obtained from the CODIF instrument (Rème et al., 1997) with a time resolution of 4.15s, and the electron data, shown in Figures 1k, 1n, 1o,1q, from the PEACE instrument (Johnstone et al., 1997) with a time resolution of 4.15s.

2.1. MMS Observations

At 14:51:30 UT (indicated as the red vertical dashed line in Figures 1d–1q MMS1 observed a dipolarization front event, inferred from the sudden increase in the B_Z component, shown in Figure 1e. Before this B_Z increase, the magnetic field was relatively quiet with a negative B_X component, indicating that MMS was located southward of the magnetic equator, which is also suggested by the TA15 model (Figures 1a–1c). In Figure 1d the electron omnidirectional energy spectrum from FPI indicates an increase in the electron energy at the DF. The ion bulk flow (Figure 1f) is increasing at about 1.5 min before the event, with the dominating component of the velocity being v_X and v_Y, indicating an earthward and duskward flow, followed by a reversal and a subsequent tailward flow. Similarly, the electron bulk flow (Figure 1g) follows the ion flow on this scales (the 4.15s resolution data shows no significant difference between the electron and ion flow)—as expected for the mesoscale (ideal MHD) bulk flow (the electron gyroperiod is on the order of 5 ms). The electron density (Figure 1h) shows a strong gradient across the DF. Several minutes before the DF event, the density was in the range of 0.5 cm^{-3}, followed by a gradual increase that is roughly in line with the bulk velocity increase, reaching a level of up to >1 cm^{-3}. An ion plasma beta of 10 (Figure 1i) before the DF indicates the MMS spacecraft's location to be in the central plasma sheet. The region behind the DF with significantly decreased beta due to the increase in total field strength and rapid density decrease is consistent with a dipolarizing flux bundle (DFB) (Liu et al., 2013). In Figure 1j the electron temperature in parallel (red) and perpendicular (black) direction is shown. During the DF the typical increase in the temperature is observed (Ohtani et al., 2004), as it can be expected since the DF is considered a boundary, separating hot and tenuous plasma from cold but dense plasma sheet plasma.

2.2. Cluster Observations

At 14:51:15 UT (indicated by the green dashed line in Figures 1d–1q Cluster 4 also observed signatures of a DF, i.e., an increase of the B_Z component of the magnetic field, a density decrease and an earthward flow. Similar to MMS, Cluster four observed a peak at higher energies directly after the DF in the DFB, indicating a higher plasma temperature inside the flux bundle, as shown in Figure 1k. Again similar to MMS, Cluster 4 observed initially relatively smooth magnetic field changes, with a positive B_X indicating that Cluster 4 was northward of the magnetic equator. The proton bulk velocity data, shown in Figure 1m, indicate an earthward and dawnward flow, starting from around 1 min before the DF, with around 250 km/s in both the v_X and v_Y component. The electron bulk velocity, v_e, at Cluster 4 in Figure 1n also shows similar changes before the DF as the proton velocity, i.e., a negative v_Y component, a positive v_X component and a relatively small v_Z component. Similar to MMS, the electron density (Figure 1o) was rather constant within the range of 0.5 and 1.0 cm^{-3} up until about 14:50:00 UT. This is followed by a density increase up to about 1.5 cm^{-3}, which is associated with a decrease in temperature (Figure 1q) and some changes in magnetic field components (Figure 1l), that is, an increase in B_Y and a decrease in B_X and B_Z, that is preceding the DF event. At the DF event at 14:51:15 UT the density at Cluster 4 decreases, although not as abruptly as at MMS. After the DF event, inside the dipolarizing flux bundle, the density decreases even further down to <0.5 cm^{-3} with its minimum at around 14:52:00 UT, along with a decrease in plasma beta (Figure 1p). At the time of the DF event the temperature increases and shows a slight anisotropy with the parallel component dominating behind the DF, similar to the MMS case.

2.3. Comparing MMS and Cluster

When the MMS and the Cluster 4 observations are compared, we notice several features that are present at both locations, observed by only a 15s difference. Both spacecraft observe a DF event with its characteristic B_Z increase. Furthermore, the temporal electron density profile is comparable in both trend and absolute numbers

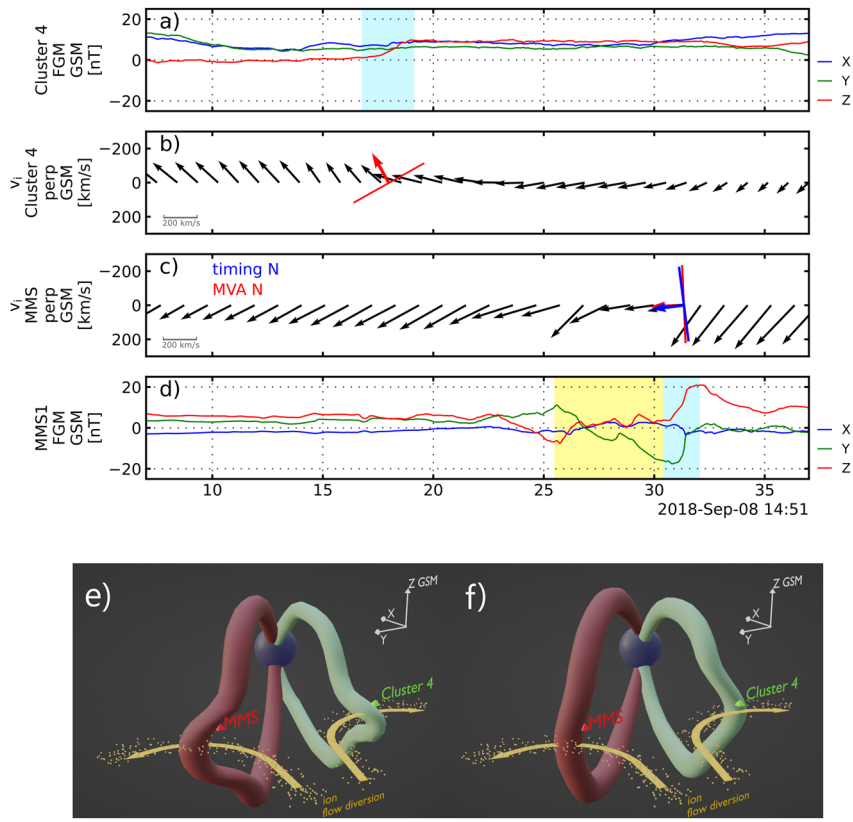

Figure 2. Comparison between MMS1 and Cluster 4 magnetic field and ion bulk flow direction and large scale situation. (a) Cluster 4 magnetic field in GSM with DF highlighted as blue shaded region, (b) Cluster four perpendicular ion bulk velocity, projected onto XY GSM plane, (c) MMS1 perpendicular ion bulk velocity, projected onto XY GSM plane, (d) MMS1 magnetic field in GSM with DF highlighted as blue shaded region, (e) 3D impression of distorted magnetic flux tube geometry due to plasma flow diversion (yellow arrows) at the position of MMS and Cluster 4 before the DF crossing, (f) and after crossing.

as both spacecraft observe an enhancement in electron density, starting around 1 min before the respective event. Due to the relatively small absolute separation of 2.6 R_E between the MMS and Cluster 4 spacecraft, and the short time difference between the DF events, we suggest that the same DF event is observed by both missions, but at a different location within the fast flow. To check whether this suggestion is plausible, we estimate the expected time delay between the MMS and Cluster observations. We first estimate the DF propagation direction and the separation between MMS and Cluster when projected onto that propagation vector, and then use the velocity from the timing method (Harvey, 1998; Plaschke et al., 2016), applied to the MMS multi-point observation, to calculate an expected travel time. For this we assume the DF to be a static structure that moves along the magnetic tension force vector toward the Earth in X/Y GSM plane, which we take from the TA15 model (Figure 1a) (~23° w.r.t the X GSM direction toward dawn direction). Along this projected direction, the MMS and Cluster spacecraft are separated by ~5,000 km. We note that the timing method only provides the velocity component along the local normal direction of the DF, which is 291 km/s in (0.9491, 0.1221, 0.2902) (X, Y, Z) GSM direction (7° duskward, i.e., the magnetic curvature and timing velocity direction differ by 23° + 7° = 30°). We therefore estimate the propagation velocity to be (291 km/s)/cos(30°) = 334 km/s and find a delay of 15s between the observations at the MMS and Cluster location, which is in good agreement with the observations.

To examine the relationship between the flow pattern and the DF, based on MMS and Cluster, we show in Figure 2 the magnetic field and the perpendicular ion flow between 14:51:08 and 14:51:37 UT for MMS1 and Cluster 4. The blue highlighted regions show the DF event period as observed by the respective spacecraft. The time range between the DF starting and ending was determined by selection criteria, which involve a minimum change, as well as a final value of the elevation angle $\theta = \tan^{-1}\left(B_Z / \sqrt{B_X^2 + B_Y^2}\right)$ and a transient B_Z increase

(>5 nT) within 10s. The criteria are given in detail in Hosner et al. (2022). The DF starting and ending times are identified as 14:51:30.40 and 32.06s UT for the MMS observation and at 14:51:16.76 and 19.14s UT for the Cluster observation. In the following, for the MMS case we denote this time range as t_{DF}. Shortly before the DF a change of sign in the B_X component took place: MMS crosses the neutral sheet from north to south as B_Y changes sign from positive to negative (The time interval is highlighted in yellow in Figure 2d. At Cluster 4 B_X stays positive without any signature of a neutral sheet crossing. Right when the DF is observed by MMS the B_Y component was strongly negative with almost −20 nT and the B_Z component small. At the DF itself the magnetic field then turns northward with a large magnetic shear angle of 73° across the boundary. We calculate the shear angle by taking the angle difference between the mean magnetic field vectors from a time window of one t_{DF} before the DF onset and after the B_Z maximum, respectively. At the position of Cluster the B_Z component increases from ∼0 nT to about 10 nT at the DF, while the B_Y component is hardly changing and stays positive. The magnetic shear angle at Cluster is therefore only 36° across the DF and is smaller compared to the MMS location. Figures 2b and 2c show the ion flow, perpendicular to the magnetic field, viewed from the north onto the X/Y GSM plane as black arrows; the Earth is to the left and dusk direction points down. The vectors normal to the DF plane, projected onto the X/Y plane are indicated in Figures 2b and 2c as red and blue arrows. To determine those normal vectors from the Cluster 4 data, we use the Minimum Variance Analysis (Sonnerup & Cahill, 1967; Sonnerup & Scheible, 1998) (red arrow). In the MMS case we additionally use the timing method (blue arrow) in combination with MVA (detailed below), using all four MMS spacecraft. In the latter case the two methods give very similar results. As the time interval for the MVA analysis we use a time twice the blue highlighted regions, given above (for MMS this is 29.57–32.89s and for Cluster this is 15.56–20.32s), because (a) of reproducibility via automated search routines, (b) to provide enough data to the MVA to produce significant results, and (c) to exclude data which might not be part of the DF in question any more. Both S/C see a strong earthward flow component (black arrows point to the left). Additionally, both MMS1 and Cluster 4 see a strong v_Y before the DF encounter, yet in the opposite directions: a duskward component for MMS1 and a dawnward component for Cluster 4. This indicates the presence of a diverging flow pattern or counter-rotating vortex flow structure, with both spacecraft being located in the opposite side. In the top-down picture MMS is in the counter-clockwise vortex and Cluster 4 is in the clockwise rotating vortex. The DF normal vectors are directed close to the flow (red arrows in Figures 2b and 2c), indicating that the DF is embedded into these flows at both locations. Due to the strong duskward flow component at the position of MMS in the southern hemisphere the flux tube will be distorted in the localized BBF, comparable to Birn and Hesse (2014) (see Figure 10b therein). We note that for such flux tubes at the dusk part of the BBF one expects B_Y to be positive in the southern hemisphere and negative in the northern hemisphere. Such a change of sign in B_Y is indeed detected by MMS when it crossed the neutral sheet, that is, we observe a correlated change of sign in B_Y and B_X in the yellow highlighted region in Figure 2d. Cluster 4, on the other hand, was at the dawn-part of the BBF in the northern hemisphere and observed positive B_Y distortion as expected from the dawnward flow. A qualitative depiction of this interpretation is shown in Figures 2e and 2f, where the flux tubes, observed by MMS and Cluster are shown in red and green, respectively. Figure 2e shows the flux tubes before the spacecraft observe the dipolarization front and Figure 2f shows the more dipolar-shaped flux tubes after the DF crossing. The yellow dots show the ion bulk flow toward Earth and its deflected motion is indicated by the yellow arrows.

Figure 3 shows high-resolution MMS1 data in the short time range 14:51:27-35UT around the sharp DF, highlighted as the blue region. The time resolution of the magnetic field data, shown in Figure 3b is 7.81 ms (128 Hz), the electron data (Figures 3a, 3c, 3e, and 3f) 30 ms (33.3 Hz), the ion data (Figures 3d and 3e) 150 ms (6.66 Hz) and the electric field data (Figures 3g and 3h) 0.122 ms (8,192 Hz), respectively. At around 14:51:31.4UT a peak (with its maximum at ∼1 keV) in the omnidirectional electron energy spectrum (Figure 3a) is visible and a general increase in the electron energy was observed, compared to a time before the DF. The electron velocity features distinct peaks, with the strongest component in the positive v_Z direction, exceeding 5,000 km/s (Figure 3c). On the other hand, the ion bulk velocity (Figure 3d) does not show any signatures of enhanced flow velocities. It can be seen that the density gradient of the DF starts well before the onset of the sharp B_Z increase. In accordance with the energy spectrum in Figure 3a an increase of the perpendicular (black) and parallel (red) electron temperature can be seen in Figure 3f. Figure 3g shows the electric field from the Electric Double Probe (EDP) instrument (Ergun et al., 2016; Lindqvist et al., 2016) in a field-aligned coordinate system. The $E_{\perp 1}$ component of this system points in the direction of $\mathbf{v}_i \times \mathbf{B}$, the $E_{\perp 2}$ component points in the direction of $\mathbf{B} \times (\mathbf{v}_i \times \mathbf{B})$ and the $E_{\parallel}$ component points parallel to $\mathbf{B}$. We observe strong peaks in the perpendicular direction of 50 mV/m and 100 mV/m, respectively, at around 14:51:31.5UT. A combined power spectral density (PSD) of the perpendicular electric

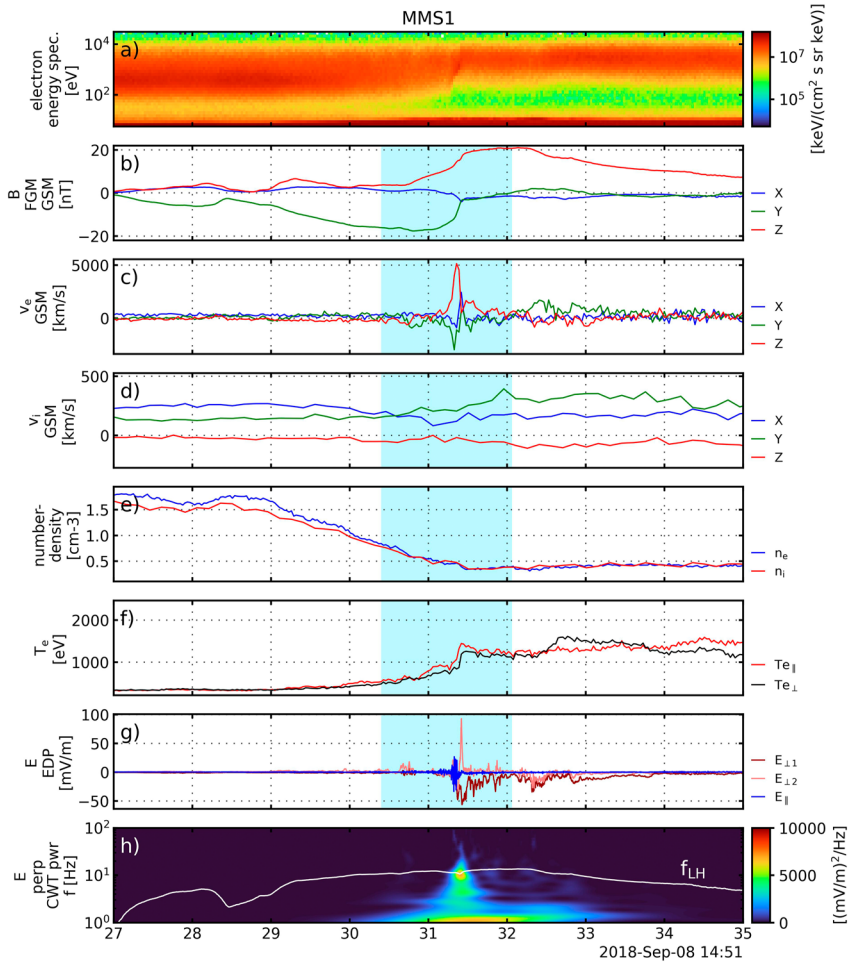

Figure 3. Flow and field changes near dipolarization front (highlighted in blue), observed by MMS1. (a) the omnidirectional electron energy spectrum, (b) the magnetic field in GSM coordinates, (c) the electron bulk velocity, (d) the ion bulk velocity, (e) the ion and electron density, (f) the perpendicular (black) and parallel (red) electron temperature, (g) the electric field in a field aligned coordinate system, where the blue component is the parallel component, $E_{\perp 1}$ point into the direction of $v_i \times B$, and $E_{\perp 2}$ in the direction of $B \times (v_i \times B)$, (h) the power spectral density obtained by the continuous wavelet transform of electric field data, together with the local lower hybrid frequency f_{LH} in white.

field components, using a continuous wavelet transform, is shown in Figure 3h. Besides a low frequency (long wavelength) component around 1 Hz, that is interpreted as the signature of the DF in the S/C frame, the PSD of the perpendicular electric field component reveals a peak at around 10 Hz, which corresponds to the local lower hybrid frequency f_{LH} (white line in Figure 3h).

3. Magnetic Field Reconstruction

In the initial work of Marshall et al. (2020) the event was interpreted as a crossing of an electron diffusion region at a dipolarization front, based on crescent-shaped electron velocity distribution and a significant electron agyrotropy and energy conversion measure **j·E'** (Zenitani et al., 2011), suggesting the presence of a reconnection site near the MMS spacecraft. The interpretation of magnetic reconnection is additionally supported after transforming the magnetic field data into an appropriate LMN system, in which a clear reversal of B_L and B_N is visible. On the other hand, Liu et al. (2022) have recently studied this event on various scales, including the electron scale where they identified a fast electron jet. However, the interpretation, in particular the reason for the acceleration of the electrons, differs from the one by Marshall et al. (2020). Rather, they concluded that the acceleration of the electrons is caused by a strong electrostatic potential that arises in the compressed flux tube but have not considered magnetic reconnection as a possible source.

The above two different interpretations can be partly due to the interpretations of the time series data from each spacecraft separately in addition to using different coordinate systems. With single-spacecraft data the depiction of the geometry, position, evolution and motion of the magnetic structure is difficult. We therefore employ a magnetic field reconstruction technique that was presented by Denton et al. (2020) to obtain information about the magnetic topology in 3D space, using all four MMS spacecraft simultaneously. The model is based on fitting a quadratic Taylor polynomial function to data of both the magnetic field measurements and electric current from particle measurements to reconstruct the magnetic field anywhere in the vicinity of the S/C formation. Since for this event, electron plasma data (and therefore the current density information) from MMS4 is not available, a solution for the fully quadratic Taylor-expansion cannot be obtained, due to lack of sufficient input data. We therefore use the Reduced Quadratic Model (RQ3D), which assumes that certain parameters of the model function are small and can be neglected. It therefore requires less input parameters and can even be used when one spacecraft out of the four does not provide particle information. In the case of the RQ3D model the parameters that are neglected are, first, the derivatives of **B** that need to be small in order to sustain a thin current sheet, and, second, parameters associated with strong changes in the out-of-plane direction. Instead of 30 unknown parameters in the fully three-dimensional quadratic Taylor expansion, those assumptions lead to a model with only 17 unknown parameters. As we investigate an active reconnection event on the scale of a few tens of electron inertial lengths (d_e), those assumptions are reasonable and the use of this model is justified. The magnetic field model is quadratic at best and the current model is linear at best.

3.1. Extension of the Method

With the RQ3D model the magnetic field data is reconstructed for any point in 3D space around the S/C. When applied to a reconnection event the X-line geometry with its typical reversal of the reconnecting field component (B_L) and normal component (B_N) can be resolved, as it was already demonstrated in the original work by Denton et al. (2020). As a next step, we use the full 3D information of the magnetic field to determine the position of the X-line in 3D space. First, we determine the orientation and location of the current sheet (CS) by searching for the plane where the B_L component reverses, that is, we search for the B_L component to change sign. For simplicity we use the magnetic field in the LN plane and search for the boundary line which separates the regions of $B_L < 0$ from $B_L > 0$. Consequently, the choice of the LMN system is critical for an accurate current sheet determination. In a second step, we search for the location of the X-line by determining the point along the CS (i.e., a line in the 2D cut), where the B_N component reverses. By applying this search routine for consecutive time steps, one can determine the motion of the X-line over time with respect to (w.r.t.) the S/C barycenter. Furthermore, we use the magnetic field topology from the reconstruction to determine the opening angle of the outflow regions, that is, the geometric angle between the separatrix field lines in the LN plane. For this purpose we first search for the separatrix field lines (or rather for field lines which we use as a proxy for the separatrix for simplicity, i.e., a field line close to the separatrix and therefore assumed to be reasonably parallel to it almost everywhere, except close to the X-point). To find such field lines, we move away from the determined X-point along L with a small but finite step length ($0.05d_e$) and calculate the field line that goes through that point in the LN plane within the reconstructed domain. Then we check the so-determined field line for a B_N reversal and repeat this process, until we find a field line that does not change sign in B_N (which is characteristic for field lines in an outflow quadrant). This field line is taken as a proxy of the separatrix field line in the respective (positive/negative) L hemisphere. Then we repeat the method for the other L direction. This way we identify a pair of field lines in the positive/negative L hemisphere, which we take as separatrix proxy. In a next step we find the orientation of the average magnetic field vector of the respective separatrix field line branches (one in each quadrant, resulting in four directions). We do this by fitting a linear function to the four branches of the separatrix field lines separately and then calculate the angles between two branches of one field line from the respective slopes of the fit. Close to the X-point the field line curvature is large due to the B_L reversal. We therefore exclude the region within $0.3d_e$ from the X-point. Since the slope of the separatrix is not linear everywhere but may vary along it, we also exclude those parts that are farther away than $3d_e$ from the X-point for the fit. Although the fit limits are determined by best guess, we found that the result of the angle depends only very weakly on them.

3.2. Application to the 2018 September 08—14:51:30 Event

We initially apply the RQ3D model to a time window between 2018/09/08 14:51:31.0 and 14:51:31.8 UT. For the actual reconstruction, and in accordance with Denton et al. (2020), we use the high resolution (128 Hz for

FGM and 30 and 150 ms for FPI) boxcar-averaged (0.3s sliding window) MMS data. The results of the RQ3D reconstruction suggests the existence of an active reconnection site. To meaningfully resolve and interpret the X-line structure we use a boundary normal LMN coordinate system. The L direction corresponds to the direction of the reconnection magnetic field, the N coordinate corresponds to the current sheet normal direction and the M component completes the right-handed coordinate system such that $L \times M = N$. We determine the LMN system by combining the timing method and the Minimum Variance Analysis (MVA), applied to data from the time interval twice as long as the DF duration (two times the blue region in Figure 3). The vector e_N is taken directly from the 4-spacecraft timing method (also shown as blue vector in Figure 2c). The vector e_L is determined by projecting the vector with the largest eigenvalue from the MVA onto the plane that is perpendicular to e_N. For the MVA method we first concatenate all the magnetic field data points of all four MMS spacecraft component-wise to one combined (B_X, B_Y, B_Z) data set, and then calculate the covariance matrix. The resulting LMN basis vectors are $e_L = [-0.3149, 0.3539, 0.8807]$, $e_M = [0.0049, -0.9273, 0.3743]$, $e_N = [0.9491, 0.1221, 0.2902]$. We note that the normal direction e_N is roughly along the DF's propagation velocity toward Earth. In Figure 4 we show the result of the reconstruction at eight different times. The times are indicated as vertical black dashed lines in Figure 4q, together with the observed magnetic field from MMS1 (solid) and MMS3 (dashed). The reconstruction in Figures 4a–4h shows the magnetic field lines in the LN plane (black lines) at an M location, given at the top of the panel. These panels are from times of crossing the reconstructed current sheet for one of the spacecraft (c–f), with additional times before (a, b) and after (g, h) the crossing of all spacecraft. The M location of the LN plane is $M = 0$ (barycenter) for panels a,b,g,h and the respective spacecraft's M location when that spacecraft crosses the center of the current sheet for the panels c–f. In the panels c–f we have also annotated the spacecraft, which's M coordinate the cut is shown in. Additional magnetic field reconstructions are shown in Supporting Information S1 (Figures S1–S5) at all four MMS spacecraft locations (and barycenter) at all aforementioned time points. The background color corresponds to the (into-plane) B_M component. The yellow line represents the current sheet of the reconnection magnetic field and the yellow X shows the position of the X-line in the shown plane. The yellow arrows indicate the direction of the magnetic field in the respective quadrant, projected onto the shown plane, for easier orientation. The spatial dimension is in units of the electron inertial length $d_e = 5.314$ km, with the origin being at the spacecraft barycenter. We can identify an X-line structure with a strong guide field (at the X-line the guide field is around 18–20 nT and $B_M/B_{L0} \sim 1.8$, with B_{L0} as the asymptotic value of B_L) at all eight shown time points in the respective LN plane. Figures 4i–4p shows the reconstruction at the same time points as before but in the LM plane and the background color corresponds to the out-of-plane B_N component. The shown N coordinate, again, corresponds to either $N = 0$ (barycenter) (Figures 4i, 4j, 4o, 4p) or the respective spacecraft's N coordinate (Figures 4k–4n) at the shown time. The green dashed lines indicate the M coordinate, at which the corresponding panels a–h are shown. The displayed colorbar limits for Figures 4i–4p are limited to ± 3 nT to highlight the B_N reversal. In the panels k, l, m, n, where the N location of the plane corresponds to one of the spacecraft's N, the B_L component at that spacecraft is negligible because the spacecraft are located near the current sheet center and the field lines are approximately parallel to the M direction, as expected. In Figures 4i–4l a second reversal of the B_N component is seen which results in an O-line structure at the positive L side w.r.t. the X-line. Possibly, similar to the situation during active magnetic substorms with multiple reconnection sites, this O-line might be confined between two X-lines (with the second one not shown) as a plasmoid, which is expelled toward the positive L direction. Figures 4k, 4l suggest that the X-line is bent in such a way that it appears to be finite. Although this may be possible, we have little further evidence for that and can as well be a consequence of the limited complexity of the model function. At a later time, represented by Figures 4m–4p, the X-line is reconstructed as a straight line in the LM plane and no second reversal in B_N is visible. One feature to note is that the X-line is not parallel to M but oblique to it (Figures 4k–4n, which shows the reconstruction in the LM plane of the current sheet). A similar slanted X-line was recently observed by Pathak et al. (2022) and Qi et al. (2023). As a consequence, the position of the X-line depends on M and the choice of the appropriate M plane for the reconstruction is therefore crucial.

The X-line mainly moves in the positive N direction w.r.t. the S/C barycenter. In Figures 4a and 4b the X-line position is at the negative N side of the four spacecraft. In Figure 4c at 14:51:31.146 UT MMS3 is crossing the reconstructed CS. MMS3's (green) and MMS4's (blue) location is roughly in the same N plane (but differ only slightly in M by $\sim 2.3 d_e \sim 12$ km) and the X-line is passing left of both MMS3 and MMS4. MMS4 is crossing the CS only ~10 ms later as shown in Figure 4d, which shows the reconstruction at the M coordinate of MMS4 at the respective crossing time of 14:51:31.156 UT. In Figure 4e the reconstructed magnetic field at the time point and M coordinate is shown, where MMS2 (red) crossed the reconstructed current sheet. Here, MMS2 is located slightly left (negative L side) of the X-line but approaches it very closely with a distance of $\sim 1 d_e$, and based on

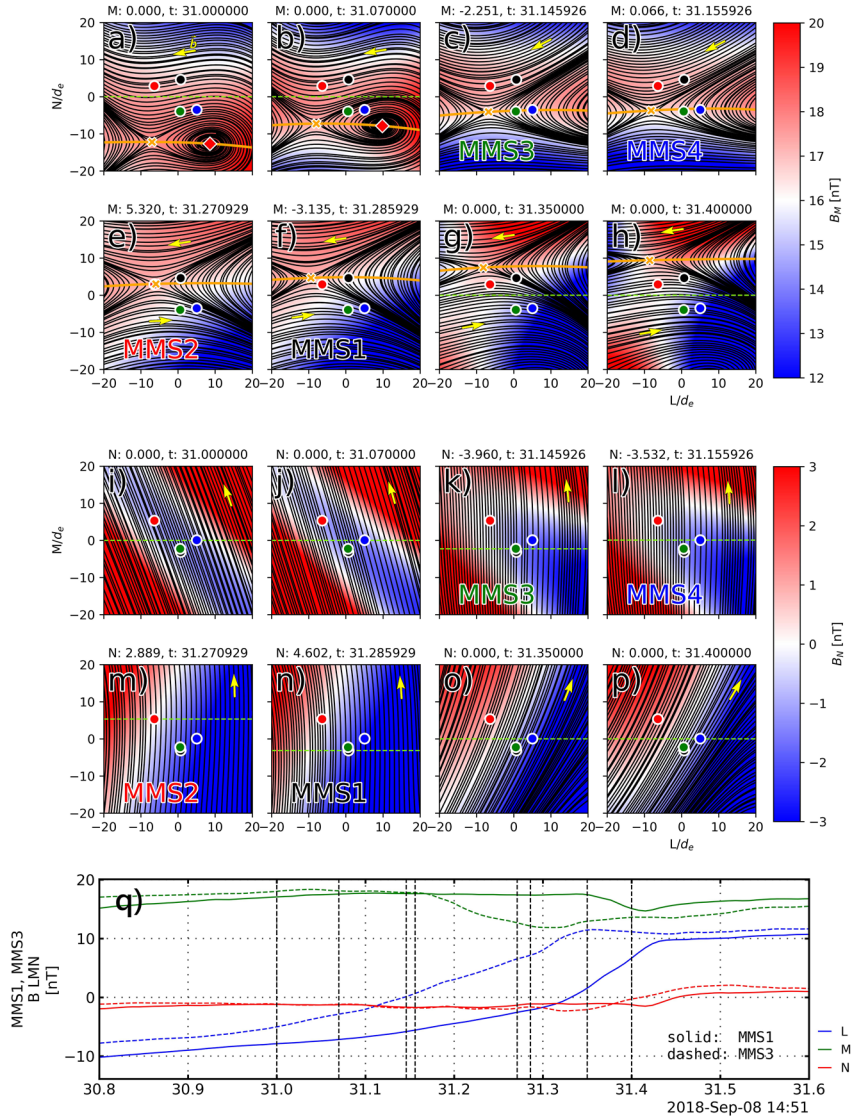

Figure 4. Result of the magnetic field reconstruction in LN and LM plane. (a)–(h) magnetic field in the LN plane, with color-coded into-plane magnetic field component B_M and current sheet center (orange line), X-line position (orange x) and O-line (red diamond), projected magnetic field vector (yellow arrows), shown N(/M) coordinate in the corresponding LM(/LN) cut (green dashed line), (c)–(f) cuts where the respective S/C is in the current sheet center, and (a,b,g,h) with S/C barycenter at times before/after the CS crossing, (i–p) same as in (a)–(h) but in the LM plane with color-coded out-of-plane B_N, (q) magnetic field observed by MMS1 (solid) and MMS3 (dashed) together with reconstructed times as vertical black dashed lines.

this reconstruction, the S/C may very well pass directly through the electron diffusion region. In Figure 4f we show the time (and M component) when MMS1 (black) crosses the reconstructed current sheet. Here, MMS1 crosses right of the X-line (positive L direction).

We further use the magnetic field reconstruction to calculate the velocity of the current sheet center in N direction w.r.t. the spacecraft barycenter, and the opening angle from the least-squares fit, as described above. The velocity of the current sheet center is determined by, first, fitting a linear function $f(L) = kL + N_0$ to the $B_L = 0$ line in the LN plane, and, second, tracking the intersection value N_0 over time, and taking the difference of them over consecutive time steps. The results are displayed in Figures 5a and 5b respectively, w.r.t time. The red curve in Figure 5a shows the current sheet center velocity, the black dashed line shows the velocity, obtained by the timing method for reference, which are in good agreement. The red shaded area around the CS center velocity shows the velocity uncertainty, resulting from uncertainties in the LMN system, which is further elaborated on

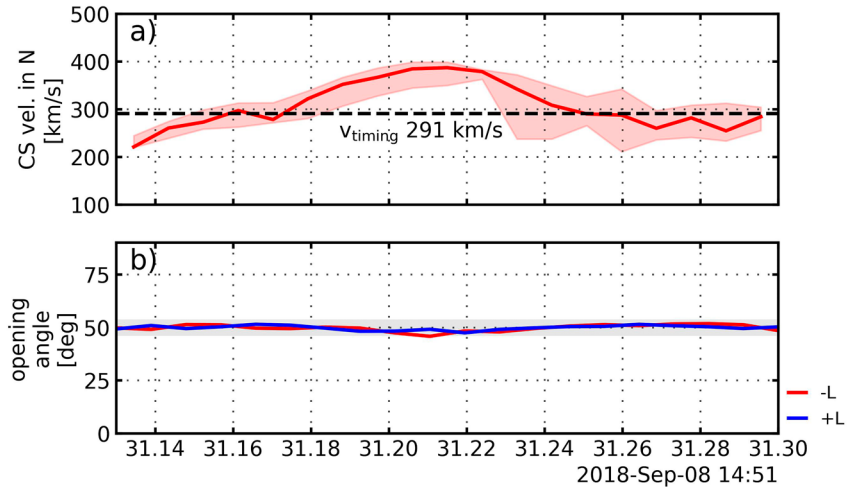

Figure 5. Current sheet propagation velocity in *N* direction obtained from reconstruction. (a) current sheet velocity w.r.t MMS spacecraft barycenter in *N* direction and timing velocity (black dashed line) and upper and lower bounds from LMN system uncertainty (red shaded area), (b) the total opening angle of the separatrices on the left (negative *L*) (red) and right (positive *L*) (blue) side and error range due to LMN system uncertainties (gray shaded area).

in the discussion section. For Figure 5 we assume an uncertainty of each unit vector of 7°. The opening angle is displayed in Figure 5b for the left (red) and right (blue) opening of the X-line and lies between 47° and 52°. The gray shaded area shows the uncertainty range (±3.9° around mean value 50°) of the opening angle, again, inferred from the LMN system uncertainty. We use the recently presented method by Liu et al. (2017),

$$R = \tan\theta\left(\frac{1-\tan^2\theta}{1+\tan^2\theta}\right)^2\sqrt{1-\tan^2\theta}, \tag{1}$$

to estimate the normalized reconnection rate R based on the X-line opening angle. We estimated $R = 0.18$ and $R = 0.16$, respectively for the minimum and maximum opening angles. In Equation 1 the opening angle θ is considered between one separatrix arm and the current sheet at the edge of the diffusion region. We note that from our method (and throughout the paper) the opening angle is considered between two separatrix arms to account for possible asymmetries. For Equation 1 we therefore use half the determined angle (i.e., between 23.5° and 26°).

3.3. Comparison With In Situ Measurements

The advantage of the magnetic field reconstruction is to visualize the field and current geometry and to deduce quantities like for example, the opening angle from geometric considerations. However, the method assumes a limited order of the Taylor polynomial model function (quadratic at most). Since the current enters into the model via $\mathrm{curl}(\mathbf{B}) = \mu_0\mathbf{j}$ (here, **B** stands for the magnetic field model function of the reconstruction and **j** is the current, obtained by particle measurements), the method requires a linear current variation in space as a consequence, to reliably reflect the underlying structure. Here, we compare the results from the reconstruction with the in situ measurements of the respective spacecraft in order to examine whether the individual field disturbances and particle signatures are consistent with the obtained X-line geometry. Figure 6 shows the MMS measurements from all four spacecraft in the LMN system. Additionally, in the respective first panel of each spacecraft (Ia-IVa), we show the temporal evolution of the reconstructed magnetic field as dashed lines for comparison. We note that for MMS4 the panels that are supposed to display the electron velocity (IVc), density (IVd) and pitch angle distributions (IVf-h) are missing due to missing data.

When we compare the temporal evolution of the magnetic field of the reconstruction and the in situ measurement of MMS1 we note several features. In Figure 6 Ia the reversal of B_L, together with a small B_N component and a strong guide field B_M component is observed. The B_N component remains negative during the CS crossing and is accompanied by a strong positive $v_{e,L} > 2{,}500$ km/s flow (Figure 6 Ic), suggesting that MMS1 passed the X-line on the positive *L* side (Figure 7). This outflow velocity in *L* can also be identified in the $E \times B$ velocity

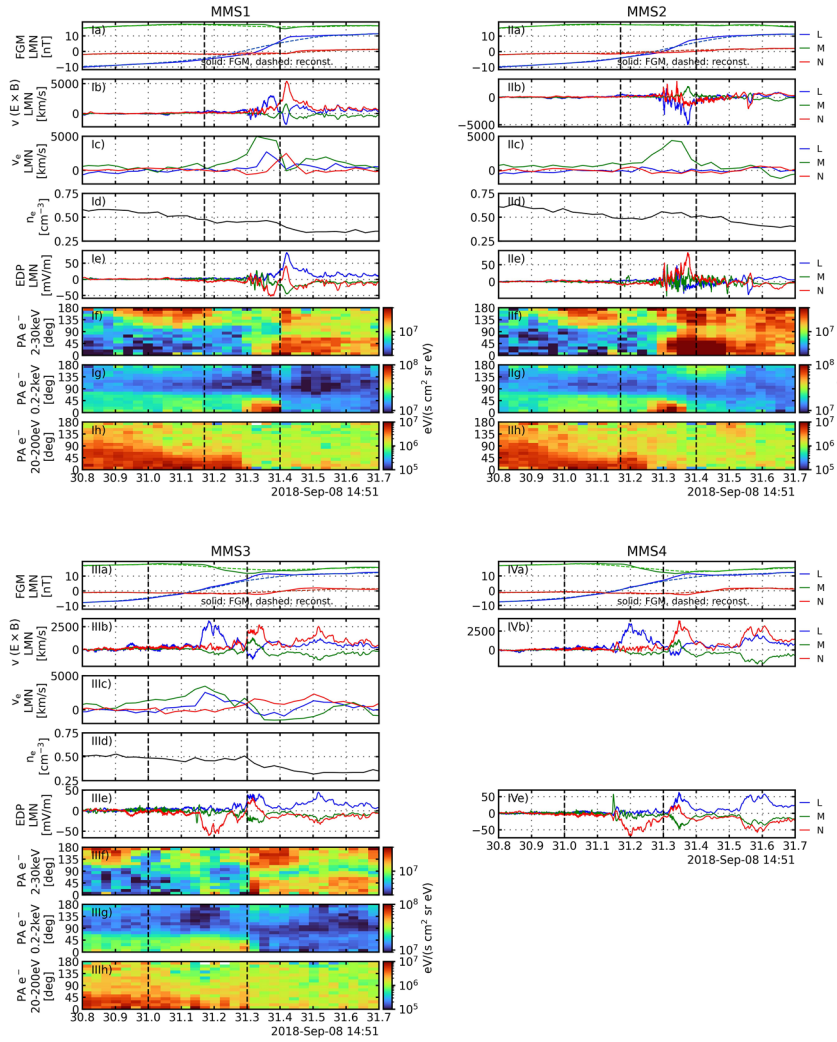

Figure 6. Field and electron data in LMN coordinates during the thin current sheet crossing plotted for the four MMS spacecraft separately, with times when the respective spacecraft enter/leave the outflow region according to the reconstruction (vertical black dashed lines). MMS1 (I), MMS2 (II), MMS3 (III), and MMS4 (IV), respectively, (a) the observed (solid) and reconstructed (dashed) magnetic field, (b) E × B velocity, (c) electron bulk velocity, (d) electron number density, (e) electric field, and (f)–(h) the pitch angle distribution for energy bins (f) 2–30 keV, (g) 0.2–2 keV, (h) 20–200 eV.

(Figure 6 Ib) during the crossing. The v_M component exceeds all other components with ∼5,000 km/s during the crossing and is not resembled by the $(E \times B)_M$ component since it is mainly a field-aligned flow, as expected in the guide-field configuration. Due to the relatively low ion velocity throughout the whole crossing (see e.g., Figure 3d), the electrons carry a strong field-aligned current component in M direction. Although the electron density generally decreases across the DF, it is constant around the time of the B_L reversal at all spacecraft, that provide data (Figures 6Id–6IIId), that is, any variations in the current density are well represented by the electron velocity and no asymmetry in the electron density across the current sheet on this scale is visible. The exhaust structure of strong guide field reconnection events was discussed in Eastwood et al. (2018) where they also observed a strong field-aligned electron flow. The peak of v_M at the negative N side (positive B_L region) is consistent with the results from guide-field reconnection simulations (Hesse et al., 2004; Pritchett & Coroniti, 2004). Although E_N is fluctuating around the center of the current sheet, the predominant negative direction at the center of the current sheet is also consistent with the prediction of the simulations. In Figure 6If-h we show the pitch angle distribution for three energy ranges (20–200 eV in h, 0.2–2 keV in g and 2–30 keV in f). Before the enhancement in v_M, starting from 14:51:31.2s UT, the parallel component of the electron distribution consists of high-energy anti field-aligned and low-energy field-aligned components. As MMS1 approaches the current

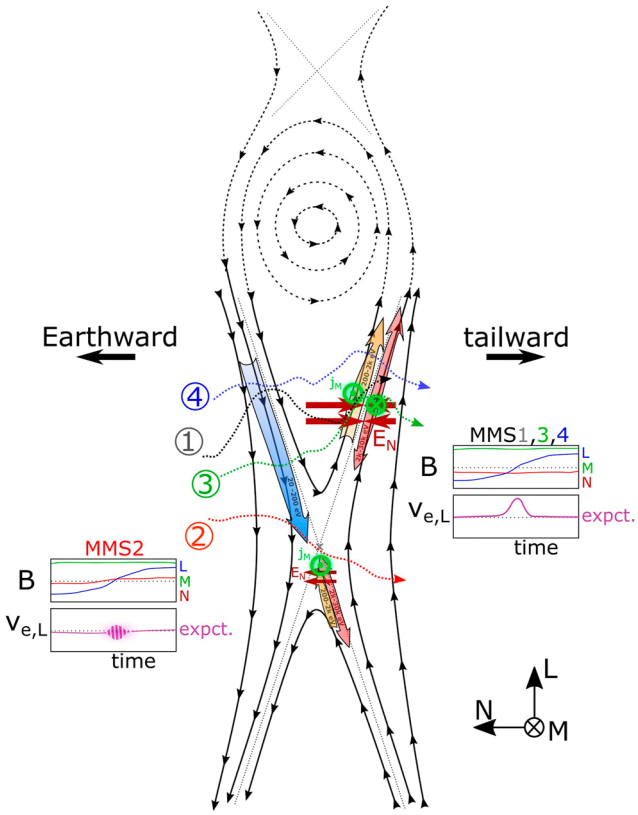

Figure 7. Schematic overview of X-line (black solid) and O-line (black dashed) geometry in LN plane, together with MMS1 (black), MMS2 (red), MMS3 (green) and MMS4 (blue) approximate trajectories based on the reconstruction. Electron flows based on PAD of energy bins 20–200 eV (blue shaded arrow), 0.2–2 keV (orange shaded arrow), 2–30 keV (red shaded arrow), observed E_N (dark red arrow), observed into-plane j_M current density (green circle/cross). Expected signature of the magnetic field in LMN coordinates and the electron outflow in L direction displayed as qualitative pseudo-time plots, as they would be observed, provided the indicated trajectory. MMS2 is indicated to be inconclusive in regards to its trajectory below/above or through the EDR.

sheet center v_M started to increase from 31.2s UT and only a low-energy parallel electron flow is visible (Figure 6 Ih), which can be interpreted as the inflow into the reconnection site along the field line (Figure 7, blue arrow). After the crossing of the current sheet center at around 31.30s UT we observe enhanced parallel components in the mid- and high-energy bins (Figure 6 If-g), while the parallel component has disappeared in the lowest energy bin (Figure 6 Ih). As the B_L component is increasing again after the CS crossing, the parallel flow also has a v_L component (at around 31.35s UT). This parallel flow is interpreted as the outflow away from the X-line, which is consistent with the position of MMS at the positive L side of the X-line. At around 31.40s UT a short enhancement in the 180° pitch-angle component (Figure 6 If), associated with a change in E_N from negative to positive (Figure 6 Ib), is observed, and v_L turns from positive to negative (Figure 6 Ib). This E_N and v_L change may suggest a weak signature of a separatrix as well as a different origin, that is, one possibility of a different origin might be another X-line close by in the positive L direction, from which those high-energy electrons may originate. When compared to the reconstruction result we note that the CS crossing takes place earlier in the reconstructed data, compared to the in situ measurement by about 48 ms (B_L reversal). Due to the boxcar-window smoothing mentioned earlier, the reconstructed B_L data is not exactly resembling the temporal variation of the in situ measurement. However, the general position of the spacecraft relative to the X-line is not heavily influenced by the smoothing because the sign on the respective B_L and B_N components at the relevant times is preserved between the smoothed and original. The reconstructed field geometry shows MMS1 on the positive L side of the X-line during its crossing of the center of the current sheet (Figure 4f), which is consistent with the in situ data.

The reconstructed as well as the observed B_N magnetic field component at MMS2 (Figure 6 IIa) that is initially negative, becomes positive and the reversal took place near the neutral sheet crossing so that MMS2 crossed closest to the X-line among the four spacecraft. Yet, there is some discrepancy for the spacecraft position relative to the X-line at the time of neutral sheet crossing. The FGM data shows a negative B_N component at the time of neutral sheet crossing that suggests the S/C to be on the positive L side of the X-line, while the reconstructed data shows a positive B_N component, suggesting the opposite. Also, the reconstruction suggests the CS crossing to happen slightly earlier than in the observational data. Nonetheless, the overall signatures were consistent with MMS2 crossing the current sheet close to the X-line from positive side of L to the negative side of L. Furthermore, when examining the velocity from particle data in Figure 6 IIc we observe the L component to be very small, in fact it is much smaller than at any other of the MMS spacecraft, and it fluctuates around zero. When looking at the pitch angle distribution in the respective energy ranges as above (Figure 6 IIf-h), we notice similar features as in the case of MMS1 before the neutral sheet crossing: low-energy electrons of pitch angles between 0° and 90° dominate, which likely represent the inflow, and v_M starts to increase when both spacecraft enter the neutral sheet. The observation of the field-aligned inflow direction is plausible, since before the X-line encounter MMS2 was still on the positive L side of the X-line. At 31.3s UT MMS2 crossed the neutral sheet, followed by a peak in v_M but no peak in v_L as in MMS1, yet the pitch angle distribution showed that MMS2 observes an electron flow in the parallel direction in all energy ranges, but also in anti-parallel direction (Figure 6 IIf-h) and the change in the energy jump in the parallel direction is less clear compared to MMS1. Based on the particle data (both moments and pitch angle) it is inconclusive on which side the MMS2 S/C passed the X-line around the neutral sheet. Yet, E_N, representing the Hall electric field, stayed positive around the v_M peak time when both the reconstructed as well as the observed B_N (hence both E_N and B_N) indicated that MMS2 was at the negative L side of the X-line. The fact that v_M is smaller (or the current density is smaller) at MMS2 compared to MMS1 suggests a weaker out-of-plane current density at the negative L side. This is also consistent with MMS1 and MMS2 being located at the opposite side of the X-line at this point. MMS2 observed a more

wave-like structure in the electric field near the neutral sheet. Consistent with the reconstruction, MMS2 is therefore assumed to cross very closely to or directly through the EDR and the bi-directional flow therefore may represent the outflow away from the X-line in both parallel and anti-parallel direction.

Data of MMS3 and the reconstruction results at the S/C's location are more consistent. Both the FGM data and the reconstruction show the B_N component to be negative, indicating the S/C to be on the positive L side of the X-line (Figure 6 IIIa). Also the time of the CS crossing between the in situ and reconstruction data is very similar. This is supported by the strong positive v_L electron flow (Figure 6 IIIc), which is comparable to the $E \times B$ drift velocity in L direction (Figure 6 IIIb and Figure 7). Also, the v_N flow component is similar to the $E \times B$ velocity. Similar to the other spacecraft we again observe the strongest component of the electron flow to be the v_M component, with velocities exceeding 2,500 km/s, that are not seen in the $E \times B$ drift. Compared to MMS2, both the in situ data and reconstruction result suggest that the spacecraft is farther away from the X-line. In Figure 6 IIIf-h, the pitch angle distributions for MMS3 are shown as before. The observed pattern is again similar to the ones observed by MMS1, except than MMS3 crossed the X-line earlier than MMS1 and MMS2. As MMS3 crosses the current sheet we observe again a mainly parallel flow (but up to ∼50°) changing toward the mid-energy range (Figure 6 IIIg), that represents the strong v_e moment in M, but also L direction at around 31.2s UT. Starting at around 31.3s UT, additionally to a parallel component, a mostly anti-parallel flow component is visible, but which also exhibits a non-negligible perpendicular part (between ∼125°–180°), shown in Figure 6 IIIf. This anti-parallel part represents the suddenly negative M component of the velocity together with the non-negligible L and N components, that are visible in the velocity moments. This coincides with the reversal of the N electric field component from negative to positive and an increase in the L electric field component, marking a crossing of a separatrix-like region as it was also visible in MMS1, which may also be due to an activation of another X-line at the positive L side.

In Figure 7 the geometrical situation is schematically depicted. It shows a qualitative X-line geometry in the LN plane, together with the trajectories of the respective four MMS spacecraft relative to the X-line. These trajectories, relative to the X-point, are loosely based on the reconstructed paths of the spacecraft in their respective LN plane. Since here the X-point serves as the origin of the coordinate system and the position of the X-point is time- and M coordinate dependent, consequently, in this picture the spacecraft trajectories do not maintain a constant separation. The respective two panels (one for MMS2 and one for MMS1,3,4, respectively) show the qualitative trend of the magnetic field and outflow velocity that is expected when the spacecraft pass at the respective side of the X-line. For a current sheet crossing at the negative L side one would expect the B_N component to be positive as well as an outflow in the negative L direction, whereas for a traversal on the positive L side, one would expect the opposite. Additionally, in accordance to the reconstruction, the cartoon indicates a possible O-line structure. The blue, orange and red arrows depict the flow along the field lines to/from the X-point. A blue arrow corresponds to the energy bin of 20–200 eV, an orange one to an energy bin of 0.2–2 keV and a red one to an energy bin of 2–30 keV, and are qualitatively deduced from the pitch angle distribution, that was observed by the spacecraft at the respective location. Also, we show the direction of E_N (and where its sign change) as indications of the regions of the spacecraft, as dark red vertical arrows. The into-plane and out-of-plane current j_M, which is mainly carried by the strong v_M electron flow, is shown in bright green. As expected from its orbit (Figure 7), MMS4 observations from electric and magnetic fields are very similar to MMS3. As stated before, the electron data are unavailable for this event, but the reconstructed and measured magnetic field data both indicate that MMS4 is on the positive L side of the X-line (Figure 6 IVa). The reconstruction in Figure 4c shows MMS4 to be even farther away from the X-line than MMS3. The structure of the electric field (and therefore the $E \times B$ velocity) is similar to the observations of MMS3, which again show a reversal in the E_N component from negative to positive, accompanied by an increase in the E_L component, suggesting a crossing of the separatrix from the outflow to the inflow region, although no particle data are available for further confirmation. Assuming that the electrons move with the $E \times B$ velocity (Figure 6 IVb) in the L and N direction, like in the case of MMS3, their flow direction further supports that MMS4 is on the positive L side of the X-line.

4. Discussion

In this work we revisit a dipolarization front event, observed by MMS in the Earth's magnetotail on 2018-09-08/14:51:30 UT that was first reported by Marshall et al. (2020). Therein, the event was interpreted as an earthward propagating flux-rope, that hosts an electron diffusion region in its core. They have investigated

the reconnection event in detail using MMS data. The same event was reported by Liu et al. (2022) on various scales to investigate cross-scale dynamics of reconnection jets. On the MHD scale this event was interpreted as a jet braking and diversion, based on MMS data. However on this length scale, when using MMS alone, a true multi-scale investigation is impossible. In the present work we study the multi-scale aspect of this event using also data from Cluster. Combining MMS and Cluster observations the large-scale context of the flow and the process that leads to the reconnection at this DF event are studied. Subsequently, the evolution of the X-line within the thin current sheet is then obtained from a detailed four-point gradient analysis of the four MMS spacecraft data to determine the reconnection parameters.

On large scales the MMS data show a dipolarization front, embedded into an earthward flow pattern that is diverging toward the dusk side. Marshall et al. (2020) suggested this event to be a flux rope-type DF with an electron-scale current sheet in its center. Indeed, reconnection between the inner magnetosphere's (northward) dipolar field and the leading edge of a flux rope's (southward) field in the magnetotail (re-reconnection) was examined by for example, Man et al. (2018), Poh et al. (2019), Vogiatzis et al. (2011), Vogiatzis et al. (2015) in the context of larger scales, and interpreted as a mechanism of flux rope erosion due to reconnection during their way toward Earth. However, when examining the magnetic field data in the interval between 14:51:28 and 14:51:32UT (Figure 2d), B_Z shows a sharp change that is correlated with a change in B_Y, in particular, B_Z increases and the magnitude of B_Y decreases from −20 to −3 nT. This indicates that the magnetic field rotates from the −Y direction to the $+Z$ direction, whereas for a flux rope one would expect a helical structure with a reversing component, together with an uncorrelated strong core field component. We therefore suggest a different configuration, that is, instead of a dawn-duskward oriented flux-rope, the observed magnetic field rather represents a duskward-bent flux tube at the MMS location, which is followed by a dipolar flux tube (Figures 2e and 2f). The boundary region between the two flux tubes (i.e., the leading edge of the following dipolar flux tube) is then interpreted as the dipolarization front. In the work of Liu et al. (2022), the large scale situation was described as a flux tube that is azimuthally bent. The magnetic field is frozen into the earthward plasma flow that diverts duskwards when approaching the Earth, distorting the embedded flux tube. In such a geometry a change of the B_Y component is then correlated with a change of sign of B_X when crossing the neutral sheet. Such a correlation between the B_Y and B_X component is indeed observed before the DF encounter (Figure 2 yellow region). There, the simultaneous change of sign of B_Y and B_X indicates the MMS spacecraft cross the neutral sheet of a duskward-distorted flux tube.

When using also Cluster data we see a dipolarization event only 15s earlier which is also embedded into a diverging flow pattern, yet the flow is going toward the dawnside. Due to similar features such as density and flow structures between the two events, as well as a consistent time delay estimation between the two locations, we interpret the two observations to represent the same DF. We suggest that the flux tube distortion due to the dawn-dusk diversion of the flow in the flow-braking region creates a magnetic shear between the ambient field and that, behind the DF. In particular the duskward flow part leads to an even larger shear at the MMS location due to a compression and a resulting flux pileup. The magnetic shear angle across the boundary at the MMS location is about twice as large as at the Cluster location. At the MMS location the B_L reversal and the small B_N component, as well as a strong non-frozen-in electron jet suggest that small-scale reconnection is happening. In the typical picture of reconnection in the tail for example, during substorm onset at the near Earth neutral line (NENL), the reconnecting field corresponds approximately to B_X. In the present situation the reconnecting current sheet is the one from the initial dipolarization front and reconnection happens right at the DF flux bundle's leading edge. In this geometry the reconnecting field is roughly oriented north-southward, with a tilt in Y due to B_M (and indeed the L vector points roughly in the Z direction). Yet, at the location of Cluster such strong magnetic shear (36°) is not observed (Figure 1). We therefore assume that the magnetic shear angle is not sufficient for reconnection to happen at the location of Cluster and a certain threshold might not be exceeded for reconnection to be triggered. One explanation was provided by Swisdak et al. (2003), who argued that, depending on the plasma beta difference across a potentially reconnecting current sheet as well as on the magnetic shear angle, strong diamagnetic drifts can occur, which may suppress reconnection. Furthermore, based on these principles, Phan et al. (2013) showed that magnetic reconnection at the magnetopause is indeed generally only observed within a certain range of plasma beta and magnetic shear angles, by investigating a database of magnetopause crossing of the THEMIS spacecraft (Angelopoulos, 2008). For the herein discussed DF observations (i.e., at the MMS and Cluster location) we calculate also the total plasma beta difference (with $\beta_{tot} = \beta_e + \beta_i$) by, first, dividing the DF B_Z time signal in two halves; from the B_Z minimum time to B_Z maximum time and splitting it in the middle, and second,

calculating the mean total plasma beta from both halves and then taking the difference. At the MMS location we find $\Delta\beta \approx 1.9$ and at the Cluster location we find $\Delta\beta \approx 6.8$ (when performing the calculation with the electron beta only, the difference is $\Delta\beta_e = 0.15$ at the location of MMS and $\Delta\beta_e = 1.44$ at the location of Cluster 4). Together with the respective magnetic shear angles, given above, and in good agreement with the results of Phan et al. (2013) (see Figures 2b and 2g therein), we find that magnetic reconnection is expected to be inhibited at the location of Cluster, while at the location of MMS it is not.

For the investigation of the field geometry and to deduce the reconnection rate we use the magnetic field information from the Reduced Quadratic Model of Denton et al. (2020). We note that the method uses a time dependent MDD-based (Shi et al., 2005) coordinate system in which the calculation is performed. This is independent of the global LMN system, in which the result is displayed. However, to correctly interpret the result, the choice of the LMN coordinate system is of course crucial. A strong guide field component makes this even more important since already a small rotation of the LMN system can lead to a significant modification of the L and N component. Furthermore, since the X-line position is obtained by searching for the B_L and B_N reversals in the 2D LN plane, a different coordinate system will therefore yield different results and may show the X-line at a wrong position relative to the spacecraft, and makes a determination of the S/C position very challenging. For determining the global LMN system we used the Timing method to determine the current sheet normal (N) and the MVA for the reconnection magnetic field direction (L). In that coordinate system we checked the relative position of the S/C to the X-line based on consistent magnetic field, electric field and particle data for MMS1, MMS3 and MMS4. However, for MMS2 we note that the reconstruction shows the spacecraft to be very close to the X-line (on the order of $\sim 1 d_e$) or even within the EDR. Together with the absence of a clear bipolar Hall field reversal, which would indicate a clear crossing of the inflow/outflow region, the side, at which MMS2 crossed the X-line is inconclusive and might further indicate a passing of the EDR, which is consistent with the findings of Marshall et al. (2020). Both the in situ data as well as the reconstruction suggest that both MMS3 and MMS4 passed by the X-line on the right side (northward, positive L). Although particle data are not available for MMS4, the electric field structure is similar to the electric field, measured by MMS3.

Since the interpretation of the data depends strongly on the used coordinate system, we estimate the uncertainty of the determined LMN system. For the uncertainty of the N direction, which was determined by the Timing method, we follow the method of Vogt et al. (2011). We use Equation 34 therein (with $L = 54$ km being the average spacecraft distance, $V = 291$ km/s boundary velocity and $\delta t = 1/128$s the FGM sample frequency), and by also taking the shape of MMS's tetrahedron into account (in particular the planarity P and elongation E), we arrive at a maximum (worst-case) uncertainty cone of 6.7° for the N vector. The L direction, however, is well determined, with eigenvalues of the MVA being (111.5, 3.4, 0.6), which have a large ratio (in particular the ratio between largest and second largest eigenvalue is $111/3.4 = 32.6$). Since B_N is so small, turning the LMN system by 6.7° (in particular around the L axis, or in other words, tilting the N vector into-plane/out-of-plane) may already lead to a change of sign in B_N, and therefore suggest the S/C to be on the other side. Indeed, since MMS2 is so close to the X-line, turning the LMN system around the L vector by only 1° may already change its side, if the crossing side was only inferred from the sign of B_N. However, the sign of $v_{e,L}$ and the electric field signatures do not change in a significant way, and the conclusion remains the same. If one assumed the case where MMS2 does pass on the positive L side, the arrows in Figure 7 would need to be drawn on the positive L side (where they would be consistent with the ones, deduced from e.g., MMS3). The small margin for uncertainty in the LMN system, together with inconclusive data regarding its crossing side w.r.t the X-line, however, demand the conclusions, drawn from MMS2 (in particular the in/outflow pattern, shown in Figure 7), to be treated with caution. The spacecraft that is the next-closest to the X-line during the current sheet crossing is MMS3. By turning the LMN system 5° around the L direction, its B_N component changes sign and lets it appear on the negative L side during the crossing. However, the strong $v_{e,L}$ component, which is not affected by such a rotation of the LMN system, is a strong indication for MMS3 to still cross on the positive L side. This demonstrates that the determination of the S/C position relative to the X-line, especially at events with strong guide field, is challenging when only using the magnetic field, and should be supported by for example, particle observations.

When investigating the pitch angle distribution (PAD) of the electrons we notice some interesting features, concerning all spacecraft. First, before the CS crossing, the PAD shows lower energy electrons between ~0° and 50°, which are likely the inflow of the reconnection site. Then, after the crossing, it shows higher energy electrons both parallel and anti-parallel to the magnetic field. Partially, they may be attributed to the reconnection outflow. However, the observed PAD shows a counter-streaming pattern, meaning that the flow, even though field aligned,

consists of a different population that originates elsewhere. One explanation is the presence of a second X-line that lies in the positive *L* direction. This would be consistent with the island structure that is seen in the magnetic field reconstruction (Figure 4), where the island is only a temporal feature, that doesn't persist over time, and gets pushed away toward the positive *L* side, similar to the substorm situation. Multiple X-lines with island structures were obtained for this event by Korovinskiy et al. (2023), using a single-spacecraft reconstruction method, based on solving the Grad-Shafranov equation (see Figure 6c therein). In their picture, which assumes steady-state structures during the S/C crossing, MMS3 supposedly crossed an O-line, whereas MMS1 did not (see Figures 6a and 6c therein). This can be interpreted as the O-line being only a temporary feature, which is consistent with our results. In this case the first X-line is dominating and the outflow of the second one is not always visible in the S/C data.

Furthermore, the outflow structure may also be explained by Hall MHD effects. An earlier work by Kleva et al. (1995) treated guide field reconnection in an MHD framework (resistive MHD, which included the resistivity and implicitly accounted for the Hall term in Ohm's law by the pressure gradient term), and explained the asymmetric outflow structure with the electron pressure gradient that accelerates the electrons parallel to the magnetic field close to the separatrix arms, while the ions flow across the magnetic field. Similarly, more recent investigations of Eastwood et al. (2010) argued that the electron outflow may be displaced in *N* direction (i.e., introducing asymmetry) due to the $\mathbf{j}_{\mathrm{Hall}} \times \mathbf{B}_{\mathrm{g}}$ electric field term (they denote $\mathbf{j}_{\mathrm{Hall}}$ the Hall current density and $\mathbf{B}_{\mathrm{g}}$ the guide field). Our observations are consistent with the ones from Eastwood et al. (2010), and the absence of visible outflow during the first separatrix crossing of MMS1 may be explained by the distorted Hall field structure due to the strong guide field, as also shown by Pritchett and Coroniti (2004). We note that guide field reconnection with density differences between the two sides of a current sheet (asymmetric current sheet) would in principle lead to a more complex asymmetric outflow structure due to both the density asymmetry and the guide field (e.g., Pritchett and Mozer (2009)). However in our case the density stays rather constant during the current sheet crossing (Figures 6I–6IIId), and no effects from the asymmetric current sheet are observed.

In this event we did not observe the ions to participate in the reconnection dynamics. This can be due to two reasons. First (similar to Farrugia et al. (2021)), the absence of ion dynamics could be explained by the close proximity of the spacecraft to the reconnection site (within the EDR). The ions are accelerated further away, in the ion diffusion region, which is not passed by the spacecraft and therefore the ion dynamics are not observed, yet may nonetheless be present. Second, it could be electron-only reconnection (e.g., Lu et al., 2021; Phan et al., 2018). In this case no fast ion jets are observed and the ion temperature does not peak (not shown), which would otherwise be expected during "standard" reconnection. Indeed we do not observe fast ion jets other than the BBF-like flows and, although the ion temperature is increasing, no clear peak is visible. This temperature increase can be attributed to the dipolarization front itself, as it poses a natural ion-scale boundary between two plasma populations and is not sufficient evidence for electron-only reconnection. Due to the lack of observational evidence, we cannot rule out either of the two and we make no statement about the participation of the ions in the reconnection process. However, the obtained reconnection rate would rather be in line with ion-coupled reconnection, than electron-only reconnection, as for the latter type, a higher reconnection rate may be expected (Pyakurel et al., 2019).

We further used the magnetic field reconstruction for determining the opening angle of the exhaust structure of the reconnecting field. This is motivated by the work of Liu et al. (2017), who connected the opening angle to the normalized reconnection rate *R* based on flux conservation considerations. The normalized reconnection rate is a measure of how efficiently the topology changes during reconnection, that is, the rate of change of magnetic flux, undergoing reconnection (e.g., Vasyliunas, 1975). Past analyses have concluded that for fast collisionless reconnection the normalized reconnection rate is on the order of $R \sim 0.1$ (Birn et al., 2001; Fuselier et al., 2010; Liu et al., 2014; Phan et al., 2001; Viavads et al., 2004). Liu et al. (2017) argued that the steady-state reconnection rate cannot differ significantly from this value due to limitations on the MHD scale, however they have found a maximum value of $R \sim 0.2$ in particle-in-cell simulations. Nakamura et al. (2018a) and Nakamura et al. (2018b) estimated the reconnection rate from the reconnection electric field, the Alfvén speed in the inflow region and the reconnecting magnetic field. Based on flux conservation, the reconnection electric field must be balanced by the inflowing magnetic flux, that is, the normalized reconnection rate can be approximated by $R \sim E_{\mathrm{r}}/(v_{\mathrm{A}}\, B_0)$, with E_{r} being the reconnection electric field (here, the out-of-plane electric field), v_{A} the upstream ion Alfvén speed and B_0 the upstream magnitude of the reconnecting magnetic field component. They found a normalized reconnection rate in the range of *R* between 0.16 and 0.20 from simulations, and successfully compared it to MMS in

situ measurements. In our study we have obtained a total opening angle between two separatrix arms between 47° and 52° during the crossing (Figure 5b), corresponding to a normalized reconnection rate of R between 0.16 and 0.18, which is in the range of previous findings. We additionally compare this method with an alternative way to obtain the opening angle and thus the reconnection rate, based on direct measurements: First, one needs to calculate the magnetic field components B_N and B_L at the edge of the EDR at the separatrix and then taking $\arctan(B_N/B_L)$ as the half opening angle. For this, the time of the separatrix crossing of a respective spacecraft must be known. We give an estimation by assuming that MMS2 passed by the edge of the EDR $1d_e$ before/after it passed the current sheet and we find the opening angle of 70°/60° respectively, which is even larger than the estimation, that the reconstruction yields. It is highlighted again, that the determination of the angle via this method strongly depends on, firstly, the LMN coordinate system and, secondly, the estimation of the edge of the EDR.

We furthermore calculate the normalized reconnection rate using the reconnection electric field from MMS2 during the crossing. Due to the strong guide field, as the reconnection electric field we take the component of $E_M{}^i$, that is parallel to the magnetic field, with $E_M{}^i = (\mathbf{E} + \mathbf{v}_i \times \mathbf{B})_M$ being the E_M component in the co-moving (ion and also the dipolarization front) frame. Here we calculated E_r from the mean value of $E_M{}^i$ from a time interval of ±0.05s around the B_L reversal. We estimate $v_A = B/\sqrt{m_i n \mu_0} = 600\,\mathrm{km/s}$ from the magnetic field and density measurements of MMS2 when the spacecraft was in the inflow region (14:51:31.20 UT, when MMS2 observed low-energy field aligned particles, see Figure 6 IIh) and use $B_0 = 10$ nT as the asymptotic value of the reconnecting field component B_L (see Figure 6 IIa). This yields an estimate of the reconnection rate of $R = 0.20$, which is in good agreement with the values obtained from the reconstruction opening angle.

This event is an example that shows that magnetic reconnection is not only taking place at the dayside magnetopause or farther down the tail at the distant or near earth neutral line during substorm onset but can also occur much closer to Earth as a consequence of interaction between the reconnection jet and the ambient magnetic field in a dynamic thin current sheet, that is, the dipolarization front. The plasma and field signatures were consistent with those predicted by the simulation of guide field magnetic reconnection (Pritchett & Coroniti, 2004; Ricci et al., 2004). Further research is needed to find evidence of thin and non frozen-in electron signatures at DFs to understand the role of these transient reconnection signatures in the overall magnetotail dynamics.

Data Availability Statement

The Magnetospheric Multiscale (MMS) data, used for data analysis in the study are publicly available at the MMS Science Data Center (SDC) via https://lasp.colorado.edu/mms/sdc/public/about/browse-wrapper/ in the Common Data Format (CDF), and can also be downloaded, using the SPEDAS (for IDL) or pySPEDAS (for Python) software. The Cluster data can be found in the Cluster Science Archive (CSA) via https://csa.esac.esa.int/csa-web/ (Laakso et al. (eds.), 2010) in various formats (such as CDF) and is available for download upon free registration. It can also be downloaded, using the SPEDAS (for IDL) or pySPEDAS (for Python) software. The magnetic field reconstruction software (Hosner & Denton, 2023) that was used for this work implements several models, which are described in Denton et al. (2020). The software itself was implemented in Python by M. Hosner and can be found at https://doi.org/10.5281/zenodo.8217728. The license can be found on the linked page.

Acknowledgments
This work was supported by the Austrian Research Fund (FWF): P32175-N27. Analysis of MMS data is partially supported by Austrian FFG projects ASAP15/873685. R. E. Denton was supported by NASA Grant 80NSSC 22K1109. The authors appreciate the helpful discussions with the ISSI team, led by E. V. Panov (Magnetotail Dipolarizations: Archimedes Force or Ideal Collapse). The authors furthermore appreciate the efforts of E. Grimes and others on the implementation and maintenance of pySPEDAS. We thank M. Kubyshkina for creating Figure 1a–c, based on the Tsyganenko and Andreeva (2015) model.

References

Alqeeq, S. W., Le Contel, O., Canu, P., Retinò, A., Chust, T., Mirioni, L., et al. (2022). Investigation of the homogeneity of energy conversion processes at dipolarization fronts from MMS measurements. *Physics of Plasmas*, *29*(1), 012906. https://doi.org/10.1063/5.0069432

Angelopoulos, V. (2008). The THEMIS mission. *Space Science Reviews*, *141*(1–4), 5–34. https://doi.org/10.1007/s11214-008-9336-1

Angelopoulos, V., Baumhojann, W., Kennel, C. F., Coroniti, F. V., Kivelson, M. G., Pellat, R., et al. (1992). Bursty bulk flows in the inner central plasma sheet. *Journal of Geophysical Research*, *97*(A4), 4027–4039. https://doi.org/10.1029/91JA02701

Angelopoulos, V., Kennel, C. F., Coroniti, F. V., Pellat, R., Kivelson, M. G., Walker, R. J., et al. (1994). Statistical characteristics of bursty bulk flow events. *Journal of Geophysical Research*, *99*(A11), 21257–21280. https://doi.org/10.1029/94JA01263

Balogh, A., Carr, C. M., Acuña, M. H., Dunlop, M. W., Book, T. J., Brown, P., et al. (2001). The cluster magnetic field investigation: Overview of in-flight performance and initial results. *Annales Geophysicae*, *19*(10/12), 1207–1217. https://doi.org/10.5194/angeo-19-1207-2001

Baumjohann, W., Paschmann, G., & Lühr, H. (1990). Characteristics of high-speed ion flows in the plasma sheet. *Journal of Geophysical Research*, *95*, 3801–3809. https://doi.org/10.1029/JA095iA04p03801

Birn, J., Drake, J. F., Shay, M. A., Rogers, B. N., Denton, R. E., Hesse, M., et al. (2001). Geospace environmental modeling (GEM) magnetic reconnection challenge. *Journal of Geophysical Research*, *106*(A3), 3715–3719. https://doi.org/10.1029/1999JA900449

Birn, J., & Hesse, M. (2014). The substorm current wedge: Further insights from MHD simulations. *Journal of Geophysical Research: Space Physics*, *119*(5), 3503–3513. https://doi.org/10.1002/2014JA019863

Burch, J. L., Moore, T. E., Torbert, R. B., & Giles, B. L. (2016). Magnetospheric Multiscale overview and science objectives. *Space Science Reviews*, *199*(1–4), 5–21. https://doi.org/10.1007/s11214-015-0164-9

Denton, R. E., Torbert, R. B., Hasegawa, H., Dors, I., Genestreti, K. J., Argall, M. R., et al. (2020). Polynomial reconstruction of the reconnection magnetic field observed by multiple spacecraft. *Journal of Geophysical Research: Space Physics*, *125*(2), e2019JA027481. https://doi.org/10.1029/2019JA027481

Divin, A., Khotyaintsev, Y. V., Viavads, A., & Andre, M. (2015). Lower hybrid drift instability at a dipolarization front. *Journal of Geophysical Research: Space Physics*, *120*(2), 1124–1132. https://doi.org/10.1002/2014JA020528

Eastwood, J. P., Mistry, R., Phan, T. D., Schwartz, S. J., Ergun, R. E., Drake, J. F., et al. (2018). Guide field reconnection: Exhaust structure and heating. *Geophysical Research Letters*, *45*(10), 4569–4577. https://doi.org/10.1029/2018GL077670

Eastwood, J. P., Shay, M. A., Phan, T. D., & Oieroset, M. (2010). Asymmetry of the ion diffusion region Hall electric and magnetic fields during guide field reconnection: Observations and comparison with simulations. *Physical Review Letters*, *104*(20), 205001. https://doi.org/10.1103/PhysRevLett.104.205001

Ergun, R. E., Tucker, S., Westfall, J., Goodrich, K. A., Malaspina, D. M., Summers, D., et al. (2016). The axial double probe and fields signal processing for the MMS mission. *Space Science Reviews*, *199*(1–4), 167–188. https://doi.org/10.1007/s11214-014-0115-x

Escoubet, C. P., Fehringer, M., & Goldstein, M. (2001). The Cluster mission. *Annales Geophysicae*, *19*(10/12), 1197–1200. https://doi.org/10.5194/angeo-19-1197-2001

Farrugia, C. J., Rogers, A. J., Torbert, R. B., Genestreti, K. J., Nakamura, T. K. M., Lavraud, B., et al. (2021). An encounter with the ion and electron diffusion regions at a flapping and twisted tail current sheet. *Journal of Geophysical Research: Space Physics*, *126*(3), e2020JA028903. https://doi.org/10.1029/2020JA028903

Fuselier, S. A., Petrinec, S. M., & Trattner, K. J. (2010). Antiparallel magnetic reconnection rates at the Earth's magnetopause. *Journal of Geophysical Research*, *115*(A10), A10207. https://doi.org/10.1029/2010JA015302

Harvey, C. C. (1998). Spatial gradients and the volumetric tensor. *ISSI Scientific Reports Series*, *1*, 307–322.

Hesse, M., Kuznetsova, M., & Birn, J. (2004). The role of electron heat flux in a guide-field magnetic reconnection. *Physics of Plasmas*, *11*(12), 5387–5397. https://doi.org/10.1063/1.1795991

Hosner, M., & Denton, R. E. (2023). Polynomial reconstruction of the magnetic field and current density - Python implementation (v1.0) [Software]. Zenodo. https://doi.org/10.5281/zenodo.8217728

Hosner, M., Nakamura, R., Nakamura, T. K. M., Schmid, D., Panov, E. V., & Plaschke, F. (2022). Statistical investigation of electric field fluctuations around the lower-hybrid frequency range at dipolarization fronts in the near-earth magnetotail. *Physics of Plasmas*, *29*(1), 012111. https://doi.org/10.1063/5.0067382

Johnstone, A. D., Alsop, C., Burge, S., Carter, P. J., Coates, A. J., Coker, A. J., et al. (1997). Peace: A plasma electron and current experiment. *Space Science Reviews*, *79*(1/2), 351–398. https://doi.org/10.1023/A:1004938001388

Kleva, R. G., Drake, J. F., & Waelbroeck, F. L. (1995). Fast reconnection in high temperature Plasmas. *Physics of Plasmas*, *2*(1), 23–34. https://doi.org/10.1063/1.871095

Korovinskiy, D., Panov, E., Nakamura, R., Kiehas, S., Hosner, M., Schmid, D., & Ivanov, I. (2023). Electron magnetohydrodynamics Grad-Shafranov reconstruction of the magnetic reconnection electron diffusion region. *Frontiers in Astronomy and Space Sciences*, *10*, 1069888. https://doi.org/10.3389/fspas.2023.1069888

Laakso, H., Perry, C., McCaffrey, S., Herment, D., Allen, A. J., Harvey, C. C., et al. (2010). Cluster active archive: Overview. In H. Laakso, M. Taylor, & C. P. Escoubet (Eds.), The cluster active archive, astrophysics and space science proceedings (pp. 3–37). Springer. 2010, [Dataset], Cluster data can be retrieved from https://csa.esac.esa.int/csa-web/

Le Contel, O., Nakamura, R., Breuillard, H., Argall, M. R., Graham, D. B., Fischer, D., et al. (2017). Lower hybrid drift waves and electromagnetic electron space-phase holes associated with dipolarization fronts and field-aligned currents observed by the magnetospheric Multiscale mission during a substorm. *Journal of Geophysical Research: Space Physics*, *122*(12), 12236–12257. https://doi.org/10.1002/2017JA024550

Lindqvist, P.-A., Olsson, G., Torbert, R. B., King, B., Granoff, M., Rau, D., et al. (2016). The spin-plane Double Probe electric field instrument for MMS. *Space Science Reviews*, *199*(1–4), 137–165. https://doi.org/10.1007/s11214-014-0116-9

Liu, C. M., Fu, H., Viavads, A., Khotyaintsev, Y. V., Gershman, D. J., Hwang, K. –J., et al. (2018a). Electron jet detected by MMS at dipolarization front. *Geophysical Research Letters*, *45*(2), 556–564. https://doi.org/10.1002/2017GL076509

Liu, C. M., Fu, H. S., Xu, Y., Khotyaintsev, Y. V., Burch, J. L., Ergun, R. E., et al. (2018b). Electron-scale measurements of dipolarization front. *Geophysical Research Letters*, *45*(10), 4628–4638. https://doi.org/10.1029/2018GL077928

Liu, C. M., Viavads, A., Khotyaintsev, Y. V., Fu, H. S., Graham, D. B., Steinvall, K., et al. (2022). Cross-scale dynamics driven by plasma jet breaking in space. *The Astrophysical Journal*, *926*(2), 198. https://doi.org/10.3847/1538-4357/ac4979

Liu, J., Angelopoulos, A., Runov, A., & Zhou, X.-Z. (2013). On the current sheets surrounding dipolarizing fluxbundles in the magnetotail: The case for wedgelets. *Journal of Geophysical Research: Space Physics*, *118*(5), 2000–2020. https://doi.org/10.1002/jgra.50092

Liu, Y. –H., Daughton, W., Karimabadi, H., Li, H., & Gary, S. P. (2014). Do dispersive waves play a role in collisionless magnetic reconnection? *Physics of Plasmas*, *21*(2), 022133. https://doi.org/10.1063/1.4865579

Liu, Y. S., Hesse, M., Guo, F., Daughton, W., Li, H., Cassak, P. A., & Shay, M. A. (2017). Why does steady-state magnetic reconnection have a maximum local rate of order 0.1? *Physical Review Letters*, *118*(8), 085101. https://doi.org/10.1103/PhysRevLett.118.085101

Lu, S., Lu, Q., Wang, R., Pritchett, P. L., Hubbert, M., Qi, Y., et al. (2021). Electron-only reconnection as a transition from quiet current sheet to standard reconnection in earth's magnetotail: Particle-In-Cell simulation and application to MMS data. *Geophysical Research Letters*, *49*(11), e2022GL098547. https://doi.org/10.1029/2022GL098547

Man, H. Y., Zhou, M., Deng, X. H., Fu, H. S., Zhong, Z. H., Chen, Z. Z., et al. (2018). In situ observation of magnetic reconnection between an earthward propagating flux rope and the geomagnetic field. *Geophysical Research Letters*, *45*(17), 8729–8737. https://doi.org/10.1029/2018GL079778

Marshall, A. T., Burch, J. L., Reiff, P. H., Webster, J. M., Torbert, R. B., Ergun, R. E., et al. (2020). Asymmetric reconnection within a flux rope-type dipolarization front. *Journal of Geophysical Research: Space Physics*, *125*(1), e2019JA027296. https://doi.org/10.1029/2019JA027296

MMS Science Data Center. MMS Science Data Center [Dataset]. for "Magnetospheric Multiscale Mission Data" Retrieved from https://lasp.colorado.edu/mms/sdc/public/about/browse-wrapper/

Nakamura, R., Baumjohann, W., Klecker, B., Bogdanova, Y., Balogh, A., Rème, H., et al. (2002). Motion of the dipolarization front during a flow burst event observed by Cluster. *Geophysical Research Letters*, *29*(20). https://doi.org/10.1029/2002GL015763

Nakamura, R., Baumjohann, W., Mouikis, C., Kistler, L. M., Runov, A., Volwerk, M., et al. (2004). Spatial scale of high-speed flows in the plasma sheet observed by Cluster. *Geophysical Research Letters*, *31*(9), L09804. https://doi.org/10.1029/2004GL019558

Nakamura, R., Baumjohann, W., Nakamura, T. K. M., Panov, E. V., Schmid, D., Varsani, A., et al. (2021). Thin current sheet behind the dipolarization front. *Journal of Geophysical Research: Space Physics*, *126*(10), e2021JA029518. https://doi.org/10.1029/2021JA029518

Nakamura, T. K. M., Genestreti, K. J., Liu, Y.-S., Nakamura, R., Teh, W. –L., Hasegawa, H., et al. (2018a). Measurement of the magnetic reconnection rate in the Earth's magnetotail. *Journal of Geophysical Research: Space Physics*, *123*(11), 9150–9168. https://doi.org/10.1029/2018JA025713

Nakamura, T. K. M., Nakamura, R., Varsani, A., Genestreti, K. J., Baumjohann, W., & Liu, Y.-H. (2018b). Remote sensing of the reconnection electric field from in situ multipoint observations of the separatrix boundary. *Geophysical Research Letters*, *45*(9), 3829–3837. https://doi.org/10.1029/2018GL078340

Nakamura, T. K. M., Umeda, T., Nakamura, R., Fu, H. S., & Oka, M. (2019). Disturbance at the front region of magnetic reconnection outflow jets due to the lower-hybrid drift instability. *Physical Review Letters*, *123*(23), 235101. https://doi.org/10.1103/PhysRevLett.123.235101

Ohtani, S. I., Shay, M. A., & Mukai, T. (2004). Temporal structure of the fast convective flow in the plasma sheet: Comparison between observations and two-fluid simulations. *Journal of Geophysical Research*, *109*(A3), A03210. https://doi.org/10.1029/2003JA010002

Pan, D.-X., Khotyaintsev, Y. V., Graham, D. B., Vaivads, A., Zhou, X.-Z., André, M., et al. (2018). Rippled electron-scale structure of a dipolarization front. *Geophysical Research Letters*, *45*(22), 12116–12124. https://doi.org/10.1029/2018GL080826

Pathak, N., Ergun, R. E., Qi, Y., Schwartz, S. J., Vo, T., Usanova, M. E., et al. (2022). Evidence of a nonorthogonal X-line in guide-field magnetic reconnection. *The Astrophysical Journal Letters*, *941*(2), L34. https://doi.org/10.3847/2041-8213/aca679

Phan, T. D., Eastwood, J. P., Shay, M. A., Drake, J. F., Sonnerup, B. U. Ö., Fujimoto, M., et al. (2018). Electron magnetic reconnection without ion coupling in Earth's turbulent magnetosheath. *Nature*, *557*(7704), 202–206. https://doi.org/10.1038/s41586-018-0091-5

Phan, T. D., Paschmann, G., Gosling, J. T., Oieroset, M., Fujimoto, M., Drake, J. F., & Angelopoulos, V. (2013). The dependence of magnetic reconnection on plasma β and magnetic shear: Evidence from magnetopause observations. *Geophysical Research Letters*, *40*(1), 11–16. https://doi.org/10.1029/2012GL054528

Phan, T. D., Sonnerup, B. U. Ö., & Lin, R. P. (2001). Fluid and kinetics signatures of reconnection at the dawn tail magnetopause: Wind observations. *Journal of Geophysical Research*, *106*(A11), 25489–25501. https://doi.org/10.1029/2001JA900054

Plaschke, F., Kahr, N., Fischer, D., Nakamura, R., Baumjohann, W., Magnes, W., et al. (2016). Steepening of waves at the duskside magneopause. *Geophysical Research Letters*, *43*(14), 7373–7380. https://doi.org/10.1002/2016GL070003

Poh, G., Slavin, J. A., Lu, S., Le, G., Ozturk, D. S., Sun, W.-J., et al. (2019). Dissipation of earthward propagating flux rope through re-reconnection with geomagnetic field: An MMS case study. *Journal of Geophysical Research: Space Physics*, *124*(9), 7477–7493. https://doi.org/10.1029/2018JA026451

Pollock, C., Moore, T., Jacques, A., Burch, J., Gliese, U., Saito, Y., et al. (2016). Fast plasma investigation for magnetospheric Multiscale. *Space Science Reviews*, *199*(1–4), 331–406. https://doi.org/10.1007/s11214-016-0245-4

Pritchett, P. L., & Coroniti, F. V. (2004). Three-dimensional collisionless magnetic reconnection in the presence of a guide field. *Journal of Geophysical Research*, *109*(A1), A01220. https://doi.org/10.1029/2003JA009999

Pritchett, P. L., & Mozer, F. S. (2009). Asymmetric magnetic reconnection in the presence of a guide field. *Journal of Geophysical Research*, *117*(A11), A11210. https://doi.org/10.1029/2009JA014343

Pyakurel, P. S., Shay, M. A., Phan, T. D., Matthaeus, W. H., Drake, J. F., TenBarge, J. M., et al. (2019). Transition from ion-coupled to electron-only reconnection: Basic physics and implications for plasma turbulence. *Physics of Plasmas*, *26*(8), 082307. https://doi.org/10.1063/1.5090403

Qi, Y., Ergun, R., Pathak, N., Li, T. C., Eriksson, S., Chasapis, A., et al. (2023). The nonorthogonal X-line in a small guide-field reconnection event in the magnetotail. *The Astrophysical Journal*, *950*(2), 168. https://doi.org/10.3847/1538-4357/acd4ba

Rème, H., Bosqued, J. M., Sauvaud, J. A., Cros, A., Dandouras, J., Aoustin, C., et al. (1997). The cluster ION spectrometry (CIS) experiment. *Space Science Reviews*, *79*(1/2), 303–350. https://doi.org/10.1023/A:1004929816409

Ricci, P., Brackbill, J. U., Daughton, W., & Lapenta, G. (2004). Collisionless magnetic reconnection in the presence of a guide field. *Physics of Plasmas*, *11*(8), 4102–4114. https://doi.org/10.1063/1.1768552

Runov, A., Angelopoulos, V., Sitnov, M. I., Sergeev, V. A., Bonnell, J., McFadden, J. P., et al. (2009). THEMIS observations of an earthward-propagating dipolarization front. *Geophysical Research Letters*, *36*(14), L14106. https://doi.org/10.1029/2009GL038980

Russell, C. T., Anderson, B. J., Baumjohann, W., Bromund, K. R., Dearborn, D., Fischer, D., et al. (2016). The magnetospheric Multiscale magnetometers. *Space Science Reviews*, *199*(1–4), 198–256. https://doi.org/10.1007/s11214-014-0057-3

Sergeev, V. A., Angelopoulos, V., Gosling, J. T., Cattell, C. A., & Russell, C. T. (1996). Detection of localized, plasma-depleted flux tubes or bubbles in the midtail plasma sheet. *Journal of Geophysical Research*, *101*(A5), 10817–10826. https://doi.org/10.1029/96JA00460

Shi, Q. Q., Shen, C., Pu, Z. Y., Dunlop, M. W., Zong, Q. –G., Zhang, H., et al. (2005). Dimensional analysis of observed structures using multipoint magnetic field measurements: Application to Cluster. *Geophysical Research Letters*, *32*(12), L12105. https://doi.org/10.1029/2005GL022454

Sonnerup, B. U. Ö., & Cahill, L. J., Jr. (1967). Magnetopause structure and attitude from Explorer 12 observations. *Journal of Geophysical Research*, *72*(1), 171–183. https://doi.org/10.1029/JZ072i001p00171

Sonnerup, B. U. Ö., & Scheible, M. (1998). Minimum and maximum variance analysis. *ISSI Scientific Reports Series*, *1*, 185–220.

Swisdak, M., Rogers, B. N., Drake, J. F., & Shay, M. A. (2003). Diamagnetic suppression of component magnetic reconnection at the magnetopause. *Journal of Geophysical Research*, *108*(A5), 1218. https://doi.org/10.1029/2002JA009726

Tsyganenko, N. A., & Andreeva, V. A. (2015). A forecasting model of the magnetosphere driven by an optimal solar wind coupling function. *Journal of Geophysical Research: Space Research*, *120*(10), 8401–8425. https://doi.org/10.1002/2015JA021641

Vasyliunas, V. M. (1975). Theoretical models of magnetic field line merging. *Reviews of Geophysics*, *13*(1), 303–336. https://doi.org/10.1029/RG013i001p00303

Viavads, A., Khotyaintsev, Y., André, M., Retinó, A., Buchert, S. C., Rogers, B. N., et al. (2004). Structure of the magnetic reconnection diffusion region from four-spacecraft observations. *Physical Review Letters*, *93*(10), 105001. https://doi.org/10.1103/PhysRevLett.93.105001

Vogiatzis, I. I., Isavnin, A., Zong, Q.-G., Sarris, E. T., Lu, S. W., & Tian, A. M. (2015). Dipolarization fronts in the near-Earth space and substorm dynamics. *Annales Geophysicae*, *33*(1), 63–74. https://doi.org/10.5194/angeo-33-63-2015

Vogiatzis, I. I., Malandraki, O. E., Zong, Q.-G., Zhou, X.-Z., Sarris, E. T., Zhang, H., & Fritz, T. A. (2011). THEMIS observations of earthward convected flux ropes triggering field dipolarization/substorm expansion and associated particle energization. *Annales Geophysicae*, *29*(11), 2117–2130. https://doi.org/10.5194/angeo-29-2117-2011

Vogt, J., Haaland, S., & Paschmann, G. (2011). Accuracy of multi-point boundary crossing time analysis. *Annales Geophysicae*, *29*(12), 2239–2252. https://doi.org/10.5194/angeo-29-2239-2011

Zenitani, S., Hesse, M., Klimas, A., & Kuznetsova, M. (2011). New measure of the dissipation region in collisionless magnetic reconnection. *Physical Review Letters*, *106*(19), 195003. https://doi.org/10.1103/PhysRevLett.106.195003